

Photoionization cross-section calculation of atomic tungsten

James J. Boyle

Institute for Theoretical Atomic and Molecular Physics, Harvard-Smithsonian Center for Astrophysics, 60 Garden Street, Cambridge, Massachusetts 02138

Zikri Altun

Department of Physics, Marmara University, Istanbul, Turkey

Hugh P. Kelly

Department of Physics, University of Virginia, Charlottesville, Virginia 22901

(Received 18 September 1992; revised manuscript received 10 February 1993)

A photoionization cross-section calculation of atomic tungsten is performed in the formalism of many-body perturbation theory for photon energies ranging from the ionization threshold of tungsten to 150 eV. Nonrelativistic orbitals are used in the basis set and relativistic corrections are included. We consider excitations from the $4f$, $5s$, $5p$, $5d$, and $6s$ subshells. The effects of the strong $5p^6 5d^4 \rightarrow 5p^5 5d^5$ and $4f^{14} 5d^4 \rightarrow 4f^{13} 5d^5$ transitions are included as resonant contributions to the $5d$ partial cross section. Our results indicate that the $5d$ partial cross section dominates the total cross section below 100 eV.

PACS number(s): 32.80.Fb

I. INTRODUCTION

A photoionization cross-section calculation of an open-shell atom can be difficult to perform when there are many strongly interacting, singly excited channels available to an outgoing electron. Typically, a large amount of computer time can be required in order to obtain a meaningful low-order result. In this work, we make use of two recently developed techniques to treat nonresonant and resonant interactions in complex, open-shell atoms. Our goal is to reduce the amount of computer time that might be needed for a photoionization cross-section calculation. The techniques that are discussed in this paper are developed from the perturbation expansion of the dipole polarizability [1].

We consider atomic tungsten, which has the LS coupled ground-state configuration $([Xe]4f^{14}5d^4 6s^2)^5D$. The label kl will denote a continuum electron orbital with linear momentum k and orbital angular momentum l in what follows. For transitions from the $5d$ subshell, there are two ionic cores: $(5d^3)^4P$ and $(5d^3)^4F$. There are five dipole-allowed channels that contribute to the $5d^4 \rightarrow 5d^3 kf$ partial cross section and that are accessible from the $(5d^3)^4P$ and $(5d^3)^4F$ ionic cores: $((5d^3)^4P; kf)^5F, ^5D$ and $((5d^3)^4F; kf)^5F, ^5D, ^5P$. Likewise, there are four dipole-allowed channels that contribute to the $5d^4 \rightarrow 5d^3 kp$ partial cross section: $((5d^3)^4P; kp)^5D, ^5P$ and $((5d^3)^4F; kp)^5F, ^5D$. We expect that there will be strong Coulomb interactions between the final channels that have the same LS couplings but that have different ionic-core couplings [2]. For the $5d^4 \rightarrow 5d^3 kl$ channels with a given l value, we are able to include a large portion of these effects into the potential function of the lowest-order Hamiltonian. Previously, this type of potential (the "effective single-particle potential" for open-shell atoms [2]) has been used in photoion-

ization calculations of chlorine [2], yttrium [3], and sulfur [4].

In addition to the class of interactions that are mentioned above, we include the effects of the strong $5p^6 5d^4 \rightarrow 5p^5 5d^5$ and $4f^{14} 5d^4 \rightarrow 4f^{13} 5d^5$ transitions in tungsten. There are nine dipole-allowed $5p^5 5d^5$ LS channels that are accessible from the $5p^6 (5d^4)^5 D_{J=0}$ initial state. The spin-orbit interaction mixes these nine dipole-allowed channels among a total of 32, $5p^5 5d^5$ LSJ channels. Likewise, there are 46, $4f^{13} 5d^5$ LSJ channels that are accessible from the $4f^{14} (5d^4)^5 D_{J=0}$ initial state through the actions of the dipole operator and the spin-orbit operator. From the $5p^5 5d^5$ and $4f^{13} 5d^5$ resonant channels that are described above, we consider 43 LSJ -coupled autoionization channels each for the $5p^5 5d^5 \rightarrow 5p^6 5d^3 kf, kp$ and $4f^{13} 5d^5 \rightarrow 4f^{14} 5d^3 kf, kp$ transitions. Our aim in this work is to include the majority of electron-correlation effects in as simple a manner as possible given the large number of resonant channels and final channels. In order to accomplish this we use the "generalized resonance" technique of Garvin [5]. This work represents the first explicit use of this technique.

There are three photoabsorption measurements of tungsten that are available for comparison with our calculation. These experimental results include an optical-absorption measurement of tungsten in the solid by Haensel *et al.* [6]; a similar measurement by Weaver and Olson [7]; and a photoabsorption measurement of laser-generated tungsten vapor performed recently by Costello *et al.* [8]. The measurements of Haensel *et al.* [6] extend over the energy region from 25 to 500 eV. The measurements of Weaver and Olson [7] and of Costello *et al.* [8] focus on the energy region of the $5p^6 5d^4 \rightarrow 5p^5 5d^5$ excitations in tungsten from 30 to 60 eV.

The formalism of many-body perturbation theory (MBPT) will be used throughout this paper. Section II

contains a short introduction to MBPT, a review of the effective single-particle potential, and a review of the generalized resonance theory. A description of the calculation and our results are presented in Sec. III. Conclusions are presented in Sec. IV.

II. THEORY

We consider the following Hamiltonian for an atom of nuclear charge Z consisting of N electrons:

$$H = H_0 + H_C + H_{SO}, \quad (1a)$$

with

$$H_0 = \sum_{i=1}^N \left[-\frac{\nabla_i^2}{2} - \frac{Z}{r_i} + V_i \right] = \sum_{i=1}^N h_i, \quad (1b)$$

$$H_C = \sum_{\substack{i,j=1 \\ (i < j)}}^N \frac{1}{r_{ij}} - \sum_{i=1}^N V_i, \quad (1c)$$

and

$$H_{SO} = \sum_{i=1}^N \zeta(r_i) l_i \cdot s_i. \quad (1d)$$

Atomic units will be used throughout this paper except where noted otherwise. The variable V_i in Eqs. (1b) and (1c) is a single-particle Hermitian potential that approximates the Coulomb repulsion between the electrons in the system. The expression in Eq. (1d) approximates the spin-orbit interaction, and $\zeta(r_i)$ is the effective spin-orbit ζ parameter that is defined by Blume and Watson [9]. We take $H_0 = \sum_{i=1}^N h_i$ as our unperturbed Hamiltonian to generate our basis orbitals ϕ and single-particle energies ϵ :

$$h_i |\phi_i\rangle = \epsilon_i |\phi_i\rangle. \quad (2)$$

We choose the normalization of our continuum orbitals ϕ_{kl} such that the radial part $R_{kl}(r)$ behaves asymptotically as

$$R_{kl}(r)|_{r \rightarrow \infty} \sim \left[\frac{1}{r} \right] \cos \left[kr + \left[\frac{q}{k} \right] \ln(2kr) - \frac{\pi}{2}(l+1) + \delta_l \right], \quad (3)$$

with $V - Z/r \sim -q/r$ as $r \rightarrow \infty$. Denoting the many-particle dipole operator by Z_{op} , the photoionization cross section for linearly polarized radiation and single-particle excitations has the following form [10,11]:

$$\sigma(\omega) = N' \sum_f \int dk \left[\frac{8\pi\omega}{ck} \right] \delta(k - \sqrt{2\omega - 2I_f}) \times \left[\langle \Psi_f | Z_{op} | \Psi_0 \rangle \right]^\dagger \langle \Psi_f | Z_{op} | \Psi_0 \rangle. \quad (4)$$

In Eq. (4), Ψ_f and Ψ_0 are the exact many-particle eigenstates of the total Hamiltonian of Eq. (1a) for the final and initial states, respectively. The variables k and l in Eqs. (3) and (4) represent the linear momentum and orbit-

al angular momentum, respectively, of the continuum electron in the final state. The incident photon energy is represented by ω , c is the speed of light, and N' is a normalization factor that is calculated perturbatively [12]. The ionization threshold for the final channel $|\Psi_f\rangle$ is represented by the variable I_f , and $\delta(x)$ is a Dirac δ function.

We are also interested in the β asymmetry parameter in the dipole approximation, which is defined through the relation

$$\frac{d\sigma(\omega)}{d\Omega} = \frac{\sigma(\omega)}{4\pi} \left[1 + \beta(\omega) \frac{3 \cos^2(\theta) - 1}{2} \right]. \quad (5)$$

In Eq. (5), θ is the angle between the polarization direction of the incident light and the direction of the ejected electron. The explicit definition of the β asymmetry parameter in terms of the dipole matrix elements $\langle \Psi_f | Z_{op} | \Psi_0 \rangle$ will be given in Sec. II C.

We will concern ourselves with the length and velocity gauges of the dipole operator Z_{op} . In the length gauge, the dipole operator is the sum of the single-particle coordinate values z_i :

$$\langle \Psi_f | Z_{op} | \Psi_0 \rangle = \left\langle \Psi_f \left| \sum_{i=1}^N z_i \right| \Psi_0 \right\rangle. \quad (6)$$

Alternatively, we can express Z_{op} in terms of the momentum operator

$$\langle \Psi_f | Z_{op} | \Psi_0 \rangle = \frac{-1}{E_f - E_0} \left\langle \Psi_f \left| \sum_{i=1}^N \frac{\partial}{\partial z_i} \right| \Psi_0 \right\rangle + O \left[\frac{E_f - E_0}{c^2} \right], \quad (7)$$

where E_f and E_0 are the energy eigenvalues of Ψ_f and Ψ_0 with respect to the Hamiltonian H . Equation (7) approximates the velocity gauge. The dipole operator in the velocity gauge, in the presence of the spin-orbit interaction H_{SO} , equals a term that is proportional to a gradient operator plus an additional term that will be neglected in this work. In Appendix A we demonstrate that the additional neglected term is $O[(E_f - E_0)/(c^2)]$. Therefore, for the largest value of the photon energy $\omega = E_f - E_0$ that we consider, the neglected term is approximately 0.03% of the dipole matrix element. A necessary, but not sufficient, condition that the bra and ket vectors in Eqs. (6) and (7) are exact eigenfunctions is for the length and velocity gauges of the dipole matrix elements to agree. In our perturbation calculation, we will obtain approximate solutions for $|\Psi_0\rangle$ and $|\Psi_f\rangle$ and Eq. (7) will not be satisfied to within the terms indicated by $O[(E_f - E_0)/(c^2)]$. Nevertheless, it is customary to associate the accuracy of the calculation with the extent of the agreement that is obtained between the length and velocity versions of the cross sections.

We will apply the many-body perturbation theory of Brueckner [13] and Goldstone [14] as it is extended to atoms [15,16] in order to correct the dipole matrix elements with respect to the correlation Hamiltonian H_C

and the spin-orbit Hamiltonian H_{SO} given above. The diagrammatic representations of some of the low-order contributions to the perturbation expansion are shown in Fig. 1. The diagrammatic notation that is used in this paper is as follows: The vertical solid lines with arrows and labels indicate orbitals in the basis set [these orbitals are the solutions to Eq. (2)], the horizontal dashed lines that end in open circles indicate dipole matrix elements, and the horizontal dashed lines that connect two sets of vertical arrows indicate Coulomb matrix elements.

Figure 1(a) represents the lowest-order dipole matrix element between the core orbital indicated by the index “ a ” and the excited orbital indicated by the index “ r .” The diagrams given in Figs. 1(b) and 1(c) are time-ordered perturbative corrections to Fig. 1(a) with respect to the Coulomb interaction. For the purpose of “time ordering,” time proceeds from the bottom of the diagrams in Fig. 1 to the top. All of the diagrams in Fig. 1 contribute to a final state that contains one net unoccupied unexcited orbital “ a ” and one net occupied excited orbital “ r .” Figures 1(d) and 1(e) are peculiar to atoms that contain open subshells in their initial states, since the existence of both the hole orbital “ a ” and the particle orbital “ a ” indicates that the $n_a l_a$ subshell is not completely filled in the initial state.

In the mathematical analogs to Figs. 1(b)–1(e) there are energy denominators that are associated with the intermediate virtual excitations. If the virtual excitation occurs “before” the dipole interactions, as in Figs. 1(c)

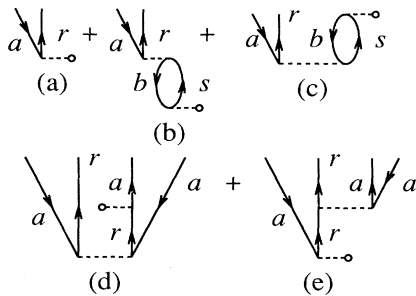


FIG. 1. A selection of low-order Brueckner-Goldstone diagrams that contribute to the dipole matrix element for photoionization. The time ordering of these diagrams proceeds from the bottom to the top. The solid lines with arrows refer to the orbitals in the basis set, and the direction of the arrow signifies the occupation status of the respective orbital. In the initial state of the system, all of the core orbitals are occupied and none of the excited orbitals are. An arrow pointing down indicates an unoccupied core orbital and an arrow pointing up indicates an occupied excited orbital. A dashed line connected to a small circle indicates a dipole interaction. A dashed line that connects two sets of arrows indicates a Coulomb interaction. The class of diagrams where a Coulomb interaction occurs after the dipole interaction in a time-ordered sense, as in Figs. 1(b) and 1(e), are referred to as “final-state correlation” diagrams. The class of diagrams where a Coulomb interaction occurs before the dipole interaction in a time-ordered sense, as in Figs. 1(c) and 1(d), are referred to as “ground-state correlation” diagrams.

and 1(d), then the general form of the energy denominator D is

$$D = \sum_{i=1}^{N_{\text{ph}}} (\varepsilon_{h_i} - \varepsilon_{p_i}), \quad (8)$$

where the variable N_{ph} represents the number of particle-hole pairs that occur in the intermediate state, ε_{h_i} is the single-particle energy of the i th hole orbital, and ε_{p_i} is the single-particle energy of the i th particle orbital. If the virtual excitation occurs “after” the dipole interaction, as in Figs. 1(b) and 1(e), then the general form of the energy denominator D is

$$D = \sum_{i=1}^{N_{\text{ph}}} (\varepsilon_{h_i} - \varepsilon_{p_i}) + \omega, \quad (9)$$

where ω is the energy of the incident photon. For example, in Fig. 1(c), the form of the energy denominator that is associated with the first-order virtual excitation is $(\varepsilon_a + \varepsilon_b - \varepsilon_r - \varepsilon_s)$, and in Fig. 1(b), the form of the energy denominator that is associated with the first-order virtual excitation is $(\varepsilon_b - \varepsilon_s + \omega)$. We notice that the energy denominators D that occur “after” the dipole interaction in Eq. (9) can vanish. These denominators are evaluated according to the rule

$$\lim_{\eta \rightarrow 0^+} (D + i\eta)^{-1} = P(D^{-1}) - i\pi\delta(D), \quad (10)$$

where P represents a principal-value integration and $\delta(D)$ represents a Dirac δ function. The limit as $\eta \rightarrow 0^+$ is taken in order to satisfy boundary conditions. Specifically, the limiting procedure arises from the requirement that the external electric field, which ionizes the atom, be turned on in an adiabatic manner from $t_0 = -\infty$ to full strength at $t = 0$ and then off again at $t = \infty$ [17].

A. The effective single-particle potential

For an atom that contains an open subshell in its initial state and is coupled to some total orbital angular momentum $L \neq 0$, there does not exist a unique LS -coupled potential for the excited orbitals in the final state [2]. An algorithm for constructing an averaged final-state potential based on MBPT was suggested by Qian, Carter, and Kelly [2]. This algorithm is based on the cancellation of the first-order many-body diagrams that appear in Fig. 2. The dashed line that is connected to a circle enclosing a bold “X” in Fig. 2 indicates an interaction with an arbitrarily defined single-particle Hermitian potential for the excited orbitals: $-V_{F(I)}$. The subscript “ $F(I)$ ” is used to identify the LS -coupled final channel that is shown below in Eq. (11c). In Ref. [2], Qian, Carter, and Kelly imposed the requirement that the first-order terms, which contribute to the “(corrections),” should sum to zero. This requirement fixes the definition of $V_{F(I)}$. Specifically, we obtain

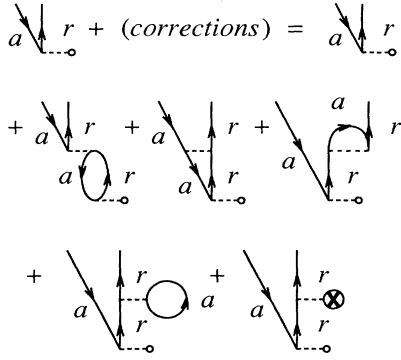


FIG. 2. The diagrams that contribute to the effective single-particle potential discussed in Sec. II A. The dashed line that is connected to a circle enclosing a bold “X” indicates an interaction with this potential. We require that the first-order terms, which contribute to the “(corrections),” should cancel. The final averaging procedure is given in Eqs. (12) and (13).

$$\begin{aligned} & \langle F(I) | V_{F(I)}(n_a l_a, k_r l_r) | F(I) \rangle \\ &= \sum_J \frac{\langle F(I) | \sum_{(i < j)} r_{ij}^{-1} | F(J) \rangle \langle F(J) | C_0^1 | G(M_L) \rangle}{\langle F(I) | C_0^1 | G(M_L) \rangle}, \end{aligned} \quad (11a)$$

with

$$|G(M_L)\rangle = |(n_a l_a)^{q_a} \alpha, L, S, M_L, M_S\rangle, \quad (11b)$$

$$|F(I)\rangle = |((n_a l_a)^{q_a - 1} \tilde{\alpha}_I \tilde{L}_I \tilde{S}_I; k_r l_r) \alpha_F, L_F, S_F, M_L, M_S\rangle, \quad (11c)$$

and C_0^1 is the spherical tensor operator appropriate to the dipole interaction [16]. In Eq. (11a) we have explicitly factored out the radial dependence of the dipole operator Z_{op} . In Eq. (11c) and throughout this paper, we use tildes over the angular momentum quantum numbers of a state in order to indicate an intermediate parent coupling. The additional I subscripts on the parent couplings that are shown in Eq. (11c) denote all of the parent states that will contribute to a final state with a total coupling L_F . We use the variable “ q_i ” to indicate the occupation number of the i th subshell $n_i l_i$ in the initial state. Equation (11a) determines the angular coefficients that are associated with $V_{F(I)}(n_a l_a, k_r l_r)$.

We remove the dependence of the matrix elements

$$\langle F(I) | V_{F(I)}(n_a l_a, k_r l_r) | F(I) \rangle$$

on the final channels by averaging with respect to the dipole matrix elements in the following manner:

$$\langle V_{LS\text{av}}(n_a l_a, k_r l_r; M_L) \rangle = \frac{\sum_{F,I} \langle G(M_L) | C_0^1 | F(I) \rangle \langle F(I) | V_{F(I)}(n_a l_a, k_r l_r) | F(I) \rangle \langle F(I) | C_0^1 | G(M_L) \rangle}{\sum_{F',I'} \langle G(M_L) | C_0^1 | F'(I') \rangle \langle F'(I') | C_0^1 | G(M_L) \rangle}. \quad (12)$$

In order to remove the M_L dependence of $\langle V_{LS\text{av}}(n_a l_a, k_r l_r; M_L) \rangle$, we define the average potential for the excited-state orbitals as

$$\langle V_{LS\text{av}}(n_a l_a, k_r l_r) \rangle = \frac{\sum_{M_L} \langle V_{LS\text{av}}(n_a l_a, k_r l_r; M_L) \rangle}{(2L + 1)}. \quad (13)$$

A more detailed description of this potential is given in Ref. [2]. Using projection-operator techniques [18], we combine the potential in Eq. (13) for the excited orbitals with a separate potential for the core orbitals into a single Hermitian potential over all of the basis orbitals. The potential that we use for the core orbitals is the restricted LS -coupled Hartree-Fock potential [16].

B. The generalized resonance technique

In this section we describe a method of incorporating the effects of resonant transitions. The resonant transitions that are of interest are indicated by the following two-step process:

$$\begin{aligned} \hbar\omega + |((n_b l_b)^{4l_b + 2} 0, 0; (n_a l_a)^{q_a} \alpha LS) \alpha LSJ\rangle &\rightarrow |((n_b l_b)^{4l_b + 1} l_b, \frac{1}{2}; (n_a l_a)^{q_a + 1} \alpha_R \underline{L}_R \underline{S}_R) \alpha_R L_R S_R J_R\rangle \\ &\rightarrow |(((n_b l_b)^{4l_b + 2} 0, 0; (n_a l_a)^{q_a - 1} \tilde{\alpha}_F \tilde{L}_F \tilde{S}_F) \tilde{\alpha}_F \tilde{L}_F \tilde{S}_F; k_F l_F) \alpha_F L_F S_F J_F\rangle. \end{aligned} \quad (14)$$

The $n_a l_a$ orbitals comprise an open subshell. The $n_b l_b$ orbitals comprise a subshell that we take to be closed ($q_b = 4l_b + 2$) and that have higher binding energies than the $n_a l_a$ orbitals. The $k_F l_F$ orbital represents a continuum-electron orbital with linear momentum k_F and orbital angular momentum l_F . As before, we use tildes over the angular

momentum quantum numbers to indicate an intermediate parent coupling. Additionally, we use tildes under the angular momentum quantum numbers in order to indicate an intermediate resonant-state coupling. We also have the identity $J_R = J_F$.

For the remainder of this paper we will use the following notation for the basis vectors of the ground state $|G(\text{GS})\rangle$, the R th resonant channel $|R^{(0)}(\text{RS})\rangle$, and the F th final channel $|F(\text{FS})\rangle$:

$$|G(\text{GS})\rangle = |((n_b l_b)^{4l_b+2} 0, 0; (n_a l_a)^{q_a} \alpha LS) \alpha LSJ\rangle, \quad (15a)$$

$$|R^{(0)}(\text{RS})\rangle = |((n_b l_b)^{4l_b+1} l_b, \frac{1}{2}; (n_a l_a)^{q_a+1} \alpha_R \underline{L}_R \underline{S}_R) \alpha_R L_R S_R J_R\rangle, \quad (15b)$$

$$|F(\text{FS})\rangle = |(((n_b l_b)^{4l_b+2} 0, 0; (n_a l_a)^{q_a-1} \tilde{\alpha}_F \tilde{L}_F \tilde{S}_F) \tilde{\alpha}_F \tilde{L}_F \tilde{S}_F; k_F l_F) \alpha_F L_F S_F J_F\rangle, \quad (15c)$$

$$H_0 |G(\text{GS})\rangle = E_G^{(0)} |G(\text{GS})\rangle, \quad (15d)$$

$$H_0 |R^{(0)}(\text{RS})\rangle = E_R^{(0)} |R^{(0)}(\text{RS})\rangle = (E_G^{(0)} - \varepsilon_b + \varepsilon_a) |R^{(0)}(\text{RS})\rangle, \quad (15e)$$

and

$$H_0 |F(\text{FS})\rangle = E_F |F(\text{FS})\rangle = \left[E_G^{(0)} + \frac{(k_F)^2}{2} - \varepsilon_a \right] |F(\text{FS})\rangle. \quad (15f)$$

The labels (GS), (RS), and (FS) stand for, respectively, ground state, resonant state, and final state.

As a generalization of the interacting resonance technique of Fliflet and Kelly [19], we consider the geometric series that is shown diagrammatically in Fig. 3:

$$T_I = T_I^{(0)} + T_I^{(1)} + \sum_J V_{IJ}^{(2)} \left[T_J^{(0)} + T_J^{(1)} + \sum_M V_{JM}^{(2)} [T_M^{(0)} + \dots] \right], \quad (16)$$

with

$$T_F^{(0)} = \langle F(\text{FS}) | Z_{\text{op}} | G(\text{GS}) \rangle, \quad (17a)$$

$$D_R^{(0)} = (E_G^{(0)} - E_R^{(0)} + \omega), \quad (17b)$$

$$T_F^{(1)} = \sum_R \frac{\left\langle F(\text{FS}) \left| \sum_{\substack{i,j \\ (i < j)}} r_{ij}^{-1} \right| R^{(0)}(\text{RS}) \right\rangle \left\langle R^{(0)}(\text{RS}) | Z_{\text{op}} | G(\text{GS}) \right\rangle}{D_R^{(0)}}, \quad (17c)$$

$$V_{IJ}^{(2)} = \sum_R \left[\frac{-2i}{|k_J|} \right] \frac{\left\langle I(\text{FS}) \left| \sum_{\substack{i,j \\ (i < j)}} r_{ij}^{-1} \right| R^{(0)}(\text{RS}) \right\rangle \left\langle R^{(0)}(\text{RS}) \left| \sum_{\substack{i,j \\ (i < j)}} r_{ij}^{-1} \right| J(\text{FS}) \right\rangle}{D_R^{(0)}}, \quad (17d)$$

and

$$T_F = \langle F(\text{FS}) | Z_{\text{op}} | G(\text{GS}) \rangle + (\text{corrections}). \quad (17e)$$

Following the example of Wendin [20], we have denoted the contribution from the Dirac δ function $-\pi\delta(D)$ in the diagrams shown in Fig. 3 by a solid horizontal line. The imaginary contribution arises from the boundary conditions that are presented in Eq. (10). In Eq. (17e), the term “(corrections)” refers to the infinite-order corrections that are contained within the geometric series of Eq. (16). In Eq. (17d), the variable $V_{IJ}^{(2)}$ is purely imaginary and the variable k_J is the linear momentum of the continuum electron in the $|J(\text{FS})\rangle$ final channel.

Equation (16) can be rewritten by multiplying on the left with $\sum_I V_{SI}^{(2)}$ and subtracting from the original series to obtain the equation

$$\sum_J [\delta(I, J) - V_{IJ}^{(2)}] T_J = T_I^{(0)} + T_I^{(1)}. \quad (18)$$

Equation (18) is a matrix equation, and each term is known except for T_J . Therefore, we can solve Eq. (18) for T_J and correct the lowest-order dipole $T_J^{(0)}$ to infinite order within this class of interactions. This is the basic generalized resonance equation that was introduced by Garvin [5]. The additional corrections that can be incorporated into Eq. (18) include the spin-orbit splitting of the resonance states, and various real energy shifts in the denominator $D_R^{(0)}$. The inclusion of these corrections is discussed below.

We begin by discussing the spin-orbit splitting of the resonance states. We use the basis set of LSJ -coupled states that span the configuration

$$((n_b l_b)^{4l_b+1}; (n_a l_a)^{q_a+1})$$

and that were introduced in Eqs. (15b) and (15e):

$$|R^{(0)}(\text{RS})\rangle = |((n_b l_b)^{4l_b+1} l_{b, \frac{1}{2}}; (n_a l_a)^{9a+1} \underline{\alpha}_R \underline{L}_R \underline{S}_R) \alpha_R L_R S_R J_R \rangle \quad (19)$$

and

$$H_0 |R^{(0)}(\text{RS})\rangle = E_R^{(0)} |R^{(0)}(\text{RS})\rangle. \quad (20)$$

Using the total Hamiltonian $H = H_0 + H_C + H_{\text{SO}}$ from Eq. (1a), we define the following matrix elements with respect to the lowest-order basis $|R^{(0)}(\text{RS})\rangle$ of Eq. (19):

$$\langle H \rangle_{IJ} = \langle I^{(0)}(\text{RS}) | H | J^{(0)}(\text{RS}) \rangle. \quad (21)$$

We are interested in forming linear combinations of the states $|R^{(0)}(\text{RS})\rangle$ that are diagonal with respect to the $\langle H \rangle_{IJ}$ matrix of Eq. (21). We will use the variable $\gamma_J^{(R)}$ to denote the mixing coefficients and we will replace the superscript “(0)” with the superscript “(1)” on the indices of the resonant states in order to denote our diagonalized resonance states: $|R^{(1)}(\text{RS})\rangle$. Therefore,

$$|R^{(1)}(\text{RS})\rangle = \sum_J |J^{(0)}(\text{RS})\rangle \gamma_J^{(R)}. \quad (22)$$

We solve for the mixing coefficients $\gamma_J^{(R)}$ and the energy eigenvalues $(E_R^{(0)} + E_R^{(1)})$ such that

$$\sum_J \langle H \rangle_{IJ} \gamma_J^{(R)} = (E_R^{(0)} + E_R^{(1)}) \gamma_I^{(R)} \quad (23)$$

or

$$\langle R^{(1)}(\text{RS}) | H | J^{(1)}(\text{RS}) \rangle = (E_R^{(0)} + E_R^{(1)}) \delta(R, J), \quad (24)$$

where $\delta(R, J)$ is a Kronecker δ between the indices “ R ” and “ J .” The eigenstates $|R^{(1)}(\text{RS})\rangle$ form an orthonormal set spanning the same space as the old basis set $|R^{(0)}(\text{RS})\rangle$. We mention that the states $|R^{(1)}(\text{RS})\rangle$ are also eigenvectors of the unperturbed Hamiltonian.

Using the diagonalized energies $E_R^{(0)} + E_R^{(1)}$, we define the following corrected energy denominator:

$$D_R^{(1)} = (E_G^{(0)} - E_R^{(0)} - E_R^{(1)} + \omega). \quad (25)$$

In our calculation, we replace the states $|R^{(0)}(\text{RS})\rangle$ with the diagonalized states $|R^{(1)}(\text{RS})\rangle$, and we replace the values of $D_R^{(0)}$ with the corrected values $D_R^{(1)}$ in Eqs. 17(b)–17(d). We will denote the matrix elements $T_{IJ}^{(1)}$ and $V_{IJ}^{(2)}$ that are corrected in this manner with bars: $\bar{T}_{IJ}^{(1)}$ and $\bar{V}_{IJ}^{(2)}$. When we use diagonalized resonance states and energy denominators, we have included terms in our perturbation expansion that correspond to final-state correlation interactions among the resonance channels [17].

In Eq. (16), we considered only the imaginary contribution $-i\pi\delta(D)$ to $V_{IJ}^{(2)}$ when we formed the matrix operator in Eq. (18). In order to complement this, according to Eq. (10), a principal-value portion $P(D^{-1})$ can be included in lowest order by calculating the real ω -dependent resonant energy shifts to the denominators $D_R^{(1)}$. The lowest-order form of the real ω -dependent resonant energy shifts will appear as

$$\Delta_R(\omega) = \sum_I \frac{2}{\pi} \text{P} \int_{k_I} dk_I \frac{\left\langle I(\text{FS}) \left| \sum_{\substack{i,j \\ (i < j)}} r_{ij}^{-1} \right| R^{(1)}(\text{RS}) \right\rangle \left\langle R^{(1)}(\text{RS}) \left| \sum_{\substack{i,j \\ (i < j)}} r_{ij}^{-1} \right| I(\text{FS}) \right\rangle}{\left[\epsilon_a - \frac{(k_I)^2}{2} + \omega \right]}, \quad (26)$$

where P denotes a principal-value integration. When we perform a simple geometric sum of this term, we obtain a shifted denominator of the form [19]

$$D_R^{(1, \omega)} = D_R^{(1)} - \Delta_R(\omega) = E_G^{(0)} - E_R^{(0)} - E_R^{(1)} - \Delta_R(\omega) + \omega. \quad (27)$$

Finally, we introduce an additional energy shift into the denominator which is a function of the total J value of the resonant states:

$$D_R^{(1, \omega, J)} = E_G^{(0)} - E_R^{(0)} - E_R^{(1)} - \Delta_R(\omega) - \Delta_R^{(\text{rel})}(J) + \omega. \quad (28)$$

The superscript “rel” is used to indicate that this number represents an absolute energy shift that is due to relativistic effects. The determination of $\Delta_R^{(\text{rel})}(J)$ will be discussed in Sec. III B. Therefore, defining

$$T_F^{(0)} = \langle F(\text{FS}) | Z_{\text{op}} | G(\text{GS}) \rangle, \quad (29a)$$

$$D_R^{(1, \omega, J)} = [E_G^{(0)} - E_R^{(0)} - E_R^{(1)} - \Delta_R(\omega) - \Delta_R^{(\text{rel})}(J) + \omega], \quad (29b)$$

$$\bar{T}_F^{(1, \omega, J)} = \sum_R \frac{\left\langle F(\text{FS}) \left| \sum_{\substack{i,j \\ (i < j)}} r_{ij}^{-1} \right| R^{(1)}(\text{RS}) \right\rangle \left\langle R^{(1)}(\text{RS}) | Z_{\text{op}} | G(\text{GS}) \right\rangle}{D_R^{(1, \omega, J)}}, \quad (29c)$$

$$\bar{V}_{IM}^{(2,\omega,J)} = \sum_R \left[\frac{-2i}{|k_M|} \right] \frac{\left\langle I(\text{FS}) \left| \sum_{\substack{i,j \\ (i < j)}} r_{ij}^{-1} \right| R^{(1)}(\text{RS}) \right\rangle \left\langle R^{(1)}(\text{RS}) \left| \sum_{\substack{i,j \\ (i < j)}} r_{ij}^{-1} \right| M(\text{FS}) \right\rangle}{D_R^{(1,\omega,J)}}, \quad (29d)$$

and

$$T_F = \langle F(\text{FS}) | Z_{\text{op}} | G(\text{GS}) \rangle + (\text{corrections}), \quad (29e)$$

the final form of the generalized resonance equation that we solve in this work is

$$\sum_M [\delta(I, M) - \bar{V}_{IM}^{(2,\omega,J)}] T_M = T_I^{(0)} + \bar{T}_I^{(1,\omega,J)}. \quad (29f)$$

A more detailed derivation of Eq. (29f) and a specific identification of the MBPT diagrams that will be accounted for by solving Eq. (29f) for the column vector T_M can be found in Boyle [17].

C. The β asymmetry parameter

In this section we present the explicit form of the β asymmetry parameter of Eq. (5) in LSJ coupling for photoexcitation transitions that leave behind the ionic core $|(n_a l_a)^{q_a-1} \tilde{\alpha} \tilde{L} \tilde{S}\rangle$ [17]:

$$\beta = \sum_{\substack{l_1, L_1, S_1, J_1 \\ l_2, L_2, J_2}} \frac{(-1)^{\tilde{L}+J_1+J_2-J_0-S_1} (30[l_1][l_2][L_1][L_2][J_1][J_2])^{1/2} \begin{Bmatrix} l_1 & l_2 & 2 \\ 0 & 0 & 0 \end{Bmatrix}}{\sum_{l', L', S', J'} M^*(l'_1, L'_1, S'_1, J'_1) M(l'_1, L'_1, S'_1, J'_1)} \times \begin{Bmatrix} L_2 & L_1 & 2 \\ l_1 & l_2 & \tilde{L} \end{Bmatrix} \begin{Bmatrix} J_2 & J_1 & 2 \\ 1 & 1 & J_0 \end{Bmatrix} \begin{Bmatrix} J_2 & J_1 & 2 \\ L_1 & L_2 & S_1 \end{Bmatrix} M(l_1, L_1, S_1, J_1) M^*(l_2, L_2, S_1, J_2), \quad (30a)$$

with

$$M(l_j, L_j, S_j, J_j) = (-i)^{l_j} \exp\{i(\delta_{l_j})\} \frac{\langle F^j(\text{FS}) | Z_{\text{op}} | G(\text{GS}) \rangle}{(-1)^{J_j - M_{J_0}} \begin{Bmatrix} 1 & J_0 & J_j \\ 0 & M_{J_0} & -M_{J_0} \end{Bmatrix}}, \quad (30b)$$

$$[x] = 2x + 1, \quad (30c)$$

$$|F^{j=1,2}(\text{FS})\rangle = |(n_a l_a)^{q_a-1} \tilde{\alpha} \tilde{L} \tilde{S}; k l_j \alpha_j L_j S_j J_j M_{J_0}\rangle, \quad (30d)$$

and

$$|G(\text{GS})\rangle = |(n_a l_a)^{q_a} \alpha_0 L_0 S_0 J_0 M_{J_0}\rangle. \quad (30e)$$

We have included the additional indices "1" and "2" on the final channel in order to indicate an independent summation over the final orbital angular momentum values of the continuum electron $|l_a \pm 1|$, where l_a is the orbital angular momentum of the ionized electron in the initial state. The variable δ_l is the total phase shift that appears in Eq. (3). The sign of the phase shift δ_l that appears in Eq. (30b) is chosen to be consistent with the incoming-wave boundary condition. Specifically, we require that the final state

$$|(n_a l_a)^{q_a-1} \tilde{\alpha} \tilde{L} \tilde{S}\rangle |\hat{\mathbf{k}}; \frac{1}{2} m_s\rangle$$

satisfy the boundary condition that at a large distance r it has the form of a plane wave plus incoming spherical waves [21]. It is important to notice that the boundary condition that was used in Eq. (10) is consistent with the boundary condition that is used in Eq. (30b) [17,22].

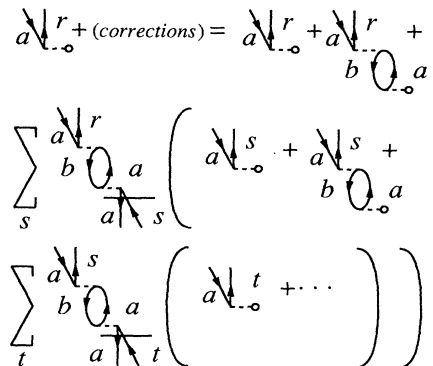


FIG. 3. The diagrams that contribute to the generalized resonance series that is discussed in Sec. II B. The exchange versions of these diagrams, although they are not shown here, are included in the calculation. Following the example of Wendin [20], we use a solid horizontal line drawn through a segment of an MBPT diagram to indicate that we are including only the imaginary contribution $-i\pi\delta(D)$ from that segment of the diagram. The imaginary contribution $-i\pi\delta(D)$ arises from the boundary conditions that are presented in Eq. (10).

III. CALCULATIONS AND RESULTS

A. The nonresonant contribution

The ground state of tungsten contains 74 electrons distributed among 14 orbitals,

$$1s^2 2s^2 2p^6 3s^2 3p^6 3d^{10} 4s^2 4p^6 4d^{10} 4f^{14} 5s^2 5p^6 5d^4 6s^2,$$

with the open $5d^4$ shell coupled to 5D (LS coupling). We expect LS coupling to dominate the angular momentum character of the $5d$ and $6s$ orbitals. In order to describe the $5p$ and inner-core orbitals accurately, the use of jj -coupled states is necessary. We took into account this aspect of the calculation by generating all of our basis orbitals in a nonrelativistic LS -coupled manner and then using parameters that were calculated relativistically for the inner-core states when it was possible. These parameters included the spin-orbit ξ parameter and an overall relativistic energy shift for the binding energy of a given inner subshell.

We considered the following photoelectric excitations into the continuum:

$$6s \rightarrow kp; 5d \rightarrow kp, kf; 5p \rightarrow ks, kd; 4f \rightarrow kd, kg; 5s \rightarrow kp. \quad (31)$$

Our core orbitals were generated using the MCHF77 computer code of Froese Fischer [23].

The continuum orbitals were calculated using the effective single-particle potential $\langle V_{LSav} \rangle$ that was discussed in Sec. II A and defined in Eqs. (11)–(13). The contributions to the potential $\langle V_{LSav} \rangle$ involving the $5d$ subshell are shown in Table I. The contributions to the potential $\langle V_{LSav} \rangle$ involving the $5s$, $5p$, $4f$, and $6s$ sub-

shells are equivalent to the usual LS -coupled potentials for transitions from closed subshells.

The thresholds for the partial photoionization cross sections were calculated by taking the difference between the self-consistent-field (SCF) calculations of the total energy of the ground state and the total energies of the ions (Δ SCF). The Δ SCF energies for the $4f$, $5s$, and $5p$ subshells were calculated using the multiconfiguration Dirac-Fock (MCDF) code of Grant *et al.* [24] and therefore include relativistic corrections. The remaining Δ SCF energies were calculated using the MCHF77 code mentioned above. The results that we obtained for the Δ SCF energies are shown in Table II.

The initial state in jj coupling should be treated as a multiconfiguration state. For the calculation of the relativistic Δ SCF energies, we assumed the initial state consisted of the following configurations:

$$|1\rangle = |(5d_{3/2}^4)J=0, M_J=0\rangle, \quad (32a)$$

$$|2\rangle = |((5d_{3/2}^2)J=0; (5d_{5/2}^2)J=0)J=0, M_J=0\rangle, \quad (32b)$$

and

$$|3\rangle = |((5d_{3/2}^2)J=2; (5d_{5/2}^2)J=2)J=0, M_J=0\rangle. \quad (32c)$$

Therefore, for the purpose of calculating the ionization thresholds in jj coupling, the initial state of tungsten had the following form:

$$|i\rangle = \alpha_1^{(i)}|1\rangle + \alpha_2^{(i)}|2\rangle + \alpha_3^{(i)}|3\rangle. \quad (32d)$$

The MCDF code operated in “optimal-level” [24] mode yielded for the ground state:

$$(\alpha_1^{(i)}, \alpha_2^{(i)}, \alpha_3^{(i)}) = (0.76893, -0.33007, 0.54754). \quad (33)$$

TABLE I. The $5d$ subshell contribution to the effective single-particle potential. The potential $\langle V_{LSav} \rangle$ was discussed in Secs. II A and III A. The contributions to the potential from the remaining subshells are equal to the usual LS -coupled potentials for transitions from closed subshells. The angular coefficients that are shown in this table were averaged in an MBPT manner and an LS -coupled manner independently as a check on their accuracy. The radial operators correspond mathematically to

$$\langle k_1 | J_{5d}^{(\kappa)} | k_2 \rangle = \int \int R_{5d}(r_1) R_{5d}(r_1) R_{k_1}(r_2) R_{k_2}(r_2) r_{<}^{\kappa} / r_{>}^{\kappa+1} r_1^2 dr_1 r_2^2 dr_2,$$

$$\langle k_1 | K_{5d}^{(\kappa)} | k_2 \rangle = \int \int R_{5d}(r_1) R_{k_1}(r_1) R_{5d}(r_2) R_{k_2}(r_2) r_{<}^{\kappa} / r_{>}^{\kappa+1} r_1^2 dr_1 r_2^2 dr_2,$$

where $r_{<}$ ($r_{>}$) indicates the lesser (greater) of r_1 and r_2 .

Radial operators	Angular coefficients to the radial operators	
	$\langle V_{LSav}(5d, kf) \rangle$	$\langle V_{LSav}(5d, kp) \rangle$
$J_{5d}^{(0)}$	3	3
$K_{5d}^{(1)}$	$\frac{131\,501}{307\,125}$	$-\frac{23}{875}$
$J_{5d}^{(2)}$	$-\frac{5912}{34\,125}$	$-\frac{867}{6125}$
$K_{5d}^{(3)}$	$-\frac{396\,456}{2\,764\,125}$	$-\frac{13\,557}{42\,875}$
$J_{5d}^{(4)}$	$-\frac{86\,361}{1\,216\,215}$	
$K_{5d}^{(5)}$	$-\frac{143\,935}{891\,891}$	

TABLE II. The Δ SCF thresholds. The thresholds for the $6s \rightarrow kp$ and the $5d \rightarrow kf, kp$ channels were calculated in a nonrelativistic LS -coupled manner using the MCHF77 [23] code. All of the other thresholds were calculated in a relativistic jj -coupled manner using the MCDF [24] code. The ionic-core couplings shown for the thresholds that were calculated relativistically indicate the largest contributor to the relativistic multiconfiguration ionic core at that energy. In the ‘‘ionic-core-coupling’’ column, the notation $((nl_j^2; j_s)J=j$ indicates the ionic coupling $((nl_j^2)J=j; (5d_{3/2}^2)J=2)J=j_s; (5d_{5/2}^2)J=2)J=j$ that is discussed in Sec. III A. The coefficients $(\lambda_r)^2$ discussed in Sec. III A are also shown in this table.

Transition channel		Δ SCF (a.u.)	$(\lambda_r)^2$	Hartree-Fock
$n_a l_a \rightarrow k_r l_r$	Ionic-core coupling			energies of ‘‘ $n_a l_a$ ’’ (a.u.)
$6s \rightarrow kp$	$((5d^4)^5 D; 6s)^6 D$	-0.1900		-0.2248
$6s \rightarrow kp$	$((5d^4)^5 D; 6s)^4 D$	-0.2495		
$5d \rightarrow kf, kp$	$(5d^3)^4 F$	-0.3692		-0.4464
$5d \rightarrow kf, kp$	$(5d^3)^4 P$	-0.4206		
$4f \rightarrow kg, kd$	$(4f_{7/2}^5; 5d_{3/2}^4)J=\frac{7}{2}$	-1.3865	0.99	-2.1997
$4f \rightarrow kg, kd$	$(4f_{5/2}^5; 5d_{3/2}^4)J=\frac{5}{2}$	-1.4794	0.99	
$5p \rightarrow kd, ks$	$(5p_{3/2}^3; 5d_{3/2}^4)J=\frac{3}{2}$	-1.6611	0.95	-1.8451
$5p \rightarrow kd, ks$	$((5p_{3/2}^3); j_s=\frac{3}{2})J=\frac{3}{2}$	-1.9012	0.04	
$5p \rightarrow kd, ks$	$((5p_{1/2}^3); j_s=\frac{5}{2})J=\frac{1}{2}$	-2.0685	0.50	
$5p \rightarrow kd, ks$	$(5p_{1/2}^3; 5d_{3/2}^4)J=\frac{1}{2}$	-2.1847	0.48	
$5p \rightarrow kd, ks$	$((5p_{1/2}^3); j_s=\frac{3}{2})J=\frac{1}{2}$	-2.2798	0.01	
$5s \rightarrow kp$	$(5s_{1/2}^1; 5d_{3/2}^4)J=\frac{1}{2}$	-3.2839	0.95	-2.9212
$5s \rightarrow kp$	$((5s_{1/2}^1); j_s=\frac{3}{2})J=\frac{1}{2}$	-3.3476	0.03	
$5s \rightarrow kp$	$((5s_{1/2}^1); j_s=\frac{5}{2})J=\frac{1}{2}$	-3.4205	0.03	

If we consider the excitations from the $4f$, $5s$, and $5p$ subshells, the states $|1\rangle$ and $|2\rangle$ in Eqs. (32a) and (32b) will have only one jj -coupled ionic core piece. This is because all of the subshells are coupled to $J=0$ for those two initial states. The state $|3\rangle$ in Eq. (32c) poses a difficulty, however, since two of the subshells within this state are coupled to $J=2$. This implies that there will be a variety of ionic-core states arising from state $|3\rangle$ that will differ in the intermediate coupling between the J coupling of the ionic core under consideration and the

$(5d_{3/2}^2)J=2$ subshell. If we denote the $4f$, $5s$, and $5p$ subshells in a general manner by the variable nl , then we can denote the final-state relativistic configurations for the channels $nl \rightarrow kj_r$ as

$$|f^{(i)}\rangle = \beta_{t1}|f_1\rangle + \beta_{t2}|f_2\rangle + \sum_{s=3}^{N_s} \beta_{ts}|f_s\rangle, \quad (34a)$$

with

$$|f_1\rangle = |(((nl_j^2)J=j; (5d_{3/2}^4)J=j; (kj_r)J=j_r)J=1, M_J=0)\rangle, \quad (34b)$$

$$|f_2\rangle = |(((nl_j^2)J=j; (5d_{3/2}^2)J=0)J=j; (5d_{5/2}^2)J=0)J=j; (kj_r)J=j_r)J=1, M_J=0)\rangle, \quad (34c)$$

and

$$|f_s\rangle = |(((nl_j^2)J=j; (5d_{3/2}^2)J=2)J=j_s; (5d_{5/2}^2)J=2)J=j; (kj_r)J=j_r)J=1, M_J=0)\rangle_{(s \geq 3)}. \quad (34d)$$

The variable n denotes the principal quantum number of the subshell we are considering excitations from and the variable l denotes the orbital angular momentum quantum number of this subshell. The subscript j on the variable l denotes the jj angular momentum value of the nl subshell and the superscript ($q=2j$) denotes the occupation number of the subshell. The variable kj_r denotes a continuum-electron orbital with the jj angular momentum value j_r . The β_{ij} are the mixing coefficients that are determined from the self-consistent calculations of the multiconfiguration ionic core and are associated with a given ionic threshold energy. Finally, the variable j_s in Eq. (34d) denotes a possible intermediate coupling between the $J=j$ state of the nl_j^2 core, and the $J=2$ state from the $5d_{3/2}$ subshell. The subscript ‘‘ s ’’ on the variable j_s acts as an index over the range of couplings that are possible. It is important to notice that the total jj coupling outside of the $5d$ subshell should match the total jj coupling inside of the $5d$ subshell for the state $|f_s\rangle$ in Eq. (34d). This condition originates from the requirement that the $5d$ subshell should act as a bystander for the first-order excitations from the other subshells. The number of possible values there are for j_s is the number of ionic cores that are available from the $|3\rangle$ state. It is shown in Appendix B that

$$\langle f^{(i)}|C_0^1|i\rangle = \langle f_1|C_0^1|1\rangle \left[\beta_{t1}\alpha_1^{(i)} + \beta_{t2}\alpha_2^{(i)} + \sum_{s=3}^{N_s} \beta_{ts}\alpha_3^{(i)}(-1)^{j-j_s} \left(\frac{2j_s+1}{5(2j+1)} \right)^{1/2} \right], \quad (35a)$$

or

$$\langle f^{(i)} | C_0^1 | i \rangle = \langle f_1 | C_0^1 | 1 \rangle \lambda_i . \quad (35b)$$

Therefore, the photoionization cross section appropriate to a given relativistic ionic threshold will be weighted by the factor $(\lambda_i)^2$. For simplicity, we rounded the values of $(\lambda_i)^2$ to the nearest 0.01, which amounts to neglecting terms of the order 0.5%. The variables $(\lambda_i)^2$ are shown in Table II. Also shown in Table II are the nonrelativistic Hartree-Fock single-particle energies used in the perturbation expansion. The β_{ij} coefficients and the corresponding ionic-core thresholds were obtained from the MCDF code operated in “average-level” [24] mode.

Figure 4 shows the lowest-order $5d$ partial cross section. This result is for the $5d^4 \rightarrow 5d^3kf$ and $5d^4 \rightarrow 5d^3kp$ transitions. The results that are shown in Fig. 4 include the corrections that are associated with using the effective single-particle potential shown in Table I and the corrections that are associated with using the $5d \rightarrow kl$ Δ SCF energies shown in Table II as the ionization thresholds.

Figure 5 shows the $5d$ partial cross section with some first-order ground- and final-state correlation corrections added to the $5d \rightarrow kf$ dipole matrix elements. The ground-state correlation effects that have been included in Fig. 5 are Fig. 1(c) with

$$(n_a l_a, k_r l_r) = (5d, kf)$$

and

$$(n_b l_b, k_s l_s) = (5d, kf), (4f, kg), (5p, kd) ,$$

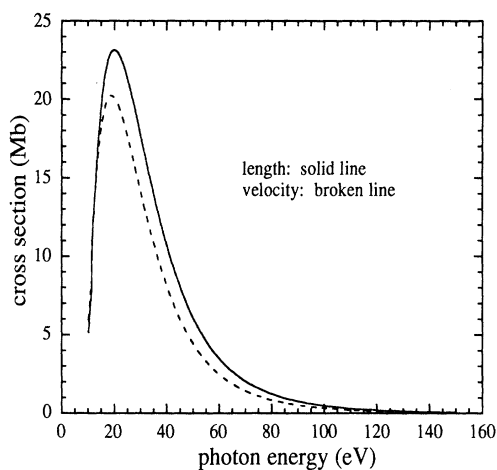


FIG. 4. The $5d$ partial photoionization cross section of tungsten in lowest order for this calculation. The solid line is the cross section that is obtained from the length gauge of the dipole operator Z_{op} and the dashed line is the cross section obtained from the velocity gauge. The effects that are included in this result are the correlations that are associated with using the effective single-particle potential from Table I and the correlations that are associated with using the $5d \rightarrow kl$ Δ SCF energies from Table II as the ionization thresholds.

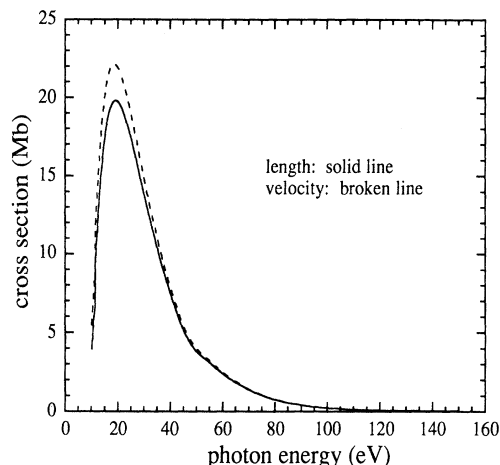


FIG. 5. The lowest-order $5d$ partial cross section with some additional first-order ground- and final-state correlation effects. The correlations that are included in this result are associated with the $5p \rightarrow kd$, $4f \rightarrow kg$, and $5d \rightarrow kf$ channels and are itemized in Sec. III A. The length form of the cross section is the solid line and the velocity form of the cross section is the dashed line.

and Fig. 1(d) with

$$(n_a l_a, k_r l_r) = (5d, kf) .$$

The final-state correlation effects that have been included in Fig. 5 are Fig. 1(b) with

$$(n_a l_a, k_r l_r) = (5d, kf)$$

and

$$(n_b l_b, k_s l_s) = (4f, kg), (5p, kd)$$

and Fig. 1(e) with

$$(n_a l_a, k_r l_r) = (5d, kf) .$$

The appropriate exchange versions of all of the MBPT diagrams that are mentioned above were also included.

The nonresonant β asymmetry parameter for the $5d$ subshell is shown in Fig. 6. The MBPT corrections that have been included in this calculation involve all of the corrections that are discussed above for Fig. 5.

The total nonresonant cross section is shown in Fig. 7. The higher-order effects that have been included in this result are the corrections that have been mentioned above for the $5d^4 \rightarrow 5d^3kf$ transitions and the corrections that are associated with using the Δ SCF energies as the ionization thresholds for the remaining partial cross sections. The $6s$, $5p$, $5s$, and $4f$ partial cross sections that are included in Fig. 7 do not incorporate any additional correlations.

One aspect of Fig. 7 which is noteworthy is the fact that the $5p$ partial cross section is small in comparison with the $5d$ partial cross section. Using the Thomas-Reiche-Kuhn sum rule [25], we would expect that the value of the total oscillator strength for the transitions from the $n = 5$ level should be 12. (This number includes

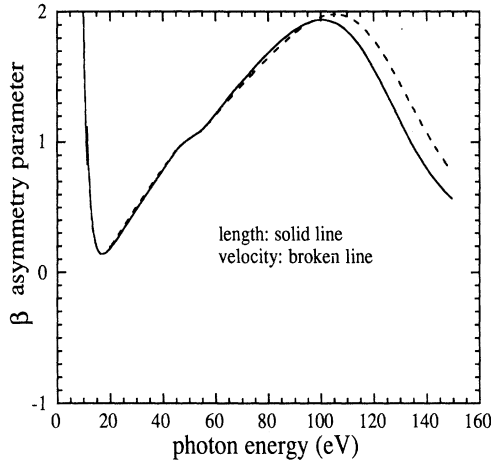


FIG. 6. The nonresonant β asymmetry for the $5d$ subshell. The MBPT corrections that have been included in this calculation involve all of the corrections that are included in Fig. 5 and are discussed in Sec. III A. The length form of the β parameter is the solid line and the velocity form of the β parameter is the dashed line.

both the bound and continuum transitions from the $n = 5$ subshell.) In our nonresonant calculation, approximately five units are contained in the $5d$ partial cross section, two units are contained in the $5p$ partial cross section, and one unit is contained in the $5s$ partial cross section. This leaves us four units of oscillator strength short. Since there is not much contribution to the oscillator strengths from the $5p \rightarrow kl$ transitions even though the $5p$ subshell contains the most electrons that are in the initial state for the $n = 5$ level, we assume that a great deal of oscillator strength will be contained in the bound transitions from the $5p$ subshell. The most significant bound transitions from the $5p$ subshell are the set of $5p^6 5d^4 \rightarrow 5p^5 5d^5$ transitions. Therefore, we would expect that the effects of the $5p^6 5d^4 \rightarrow 5p^5 5d^5$ resonant transitions on the $5d^4 \rightarrow 5d^3 kl$ transitions would affect the cross section shown in Fig. 7 appreciably.

B. The resonant contribution

For this portion of the calculation, we considered intermediate coupling in the initial state of tungsten over the five LSJ states

$$(\alpha_1^{(i)}, \alpha_2^{(i)}, \alpha_3^{(i)}, \alpha_4^{(i)}, \alpha_5^{(i)}) = (0.92519, -0.27473, 0.24907, -0.04549, 0.06662). \quad (37)$$

We used a spin-orbit mixed initial state in this portion of the calculation in order to balance some of the correlations that are included by using the spin-orbit mixed resonance states of Eq. (22): $|R^{(1)}(\text{RS})\rangle$. From the mixing coefficients that are shown in Eq. (37), we can see that the order-of-magnitude correction to the $5d^4[{}^5D_{J=0}]$ cou-

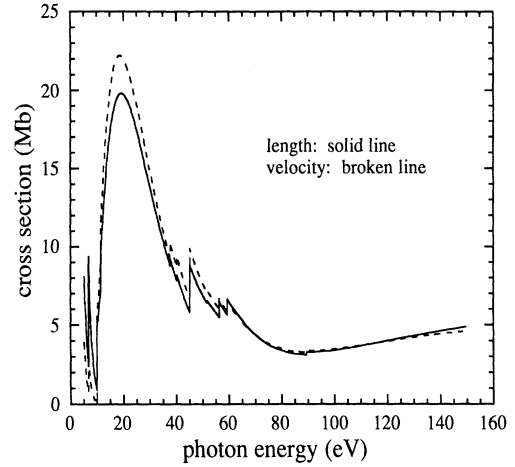


FIG. 7. The total nonresonant cross section in the length form (solid line) and the velocity form (dashed line). The $5d$ partial cross section that is shown in this figure includes the correlations that are discussed in Fig. 5. The remaining partial cross sections use the ΔSCF energies from Table II as the ionization thresholds with the appropriate weighting factors $(\lambda_r)^2$. The $6s$, $5p$, $5s$, and $4f$ partial cross sections that are shown in this figure do not include any higher-order correlations.

$$|1\rangle = |(5d^4) {}^5D_{J=0}\rangle, \quad (36a)$$

$$|2\rangle = |(5d^4) {}^3P_{J=0}\rangle, \quad (36b)$$

$$|3\rangle = |(5d^4) {}^3P_{J=0}\rangle, \quad (36c)$$

$$|4\rangle = |(5d^4) {}^1S_{J=0}\rangle, \quad (36d)$$

and

$$|5\rangle = |(5d^4) {}^1S_{J=0}\rangle. \quad (36e)$$

Therefore, our initial state of tungsten had the following form:

$$|i\rangle = \alpha_1^{(i)}|1\rangle + \alpha_2^{(i)}|2\rangle + \alpha_3^{(i)}|3\rangle + \alpha_4^{(i)}|4\rangle + \alpha_5^{(i)}|5\rangle. \quad (36f)$$

The presubscripts in Eqs. (36a)–(36e) are Racah seniority numbers. When we diagonalized the states in Eq. (36) with respect to the total spin-orbit Hamiltonian of Eq. (1), $H = H_0 + H_C + H_{\text{SO}}$, we obtained the following mixing coefficients for the ground state of tungsten:

pling by using the spin-orbit mixed initial state is

$$100\% \times [1 - (0.925)^2] \approx 14\%.$$

The resonant transitions that we consider in tungsten are the set of $5p^6 5d^4 \rightarrow 5p^5 5d^5$ and $4f^{14} 5d^4 \rightarrow 4f^{13} 5d^5$

transitions. There are 32 $J=1$ LSJ $5p^5 5d^5$ channels and 46 $J=1$ LSJ $4f^{13} 5d^5$ channels that are accessible through the dipole interaction from the $J=0$ initial state:

$$|G(\text{GS})\rangle = |5d^4[{}^5D, {}^3P, {}^3P, {}^1S, {}^1S]_{J=0}\rangle.$$

The LSJ couplings that are mentioned above for the $5p^5 5d^5$ and the $4f^{13} 5d^5$ states are used in the diagonalization of the total spin-orbit Hamiltonian $\langle H \rangle_{IJ}$ according to the description that was given in Eqs. (19) to (25). The specific itemization of the LSJ couplings of the resonant states has been given by Boyle [17].

The excited $5d$ orbitals and the relaxed $6s$ orbitals that are calculated within the $5p^5 5d^5$ and $4f^{13} 5d^5$ configurations will be denoted, respectively, by $5d_{(5p)}^*$, $5d_{(4f)}^*$ and $6s_{(5p)}^*$, $6s_{(4f)}^*$. The LSJ coupling in which we chose to generate our $5d_{(5p)}^*$ and $6s_{(5p)}^*$ orbitals was $[5p^5; (5d^5)^4G]^5F_{J=1}$, with the $5p$ and inner-core orbitals kept frozen from the ground state. The LSJ coupling in which we chose to generate our $5d_{(4f)}^*$ and $6s_{(4f)}^*$ orbitals was $[4f^{13}; (5d^5)^4G]^5D_{J=1}$, again with the $5p$ and inner-core orbitals kept frozen from the ground state. The $5d^*$ and $6s^*$ orbitals that are mentioned above were generated using the MCHF77 code [23]. We found the overlap integrals to be

$$\langle 5d_{(5p)}^* | 5d \rangle = 0.9998,$$

$$\langle 6s_{(5p)}^* | 6s \rangle = 0.9995,$$

$$\langle 5d_{(4f)}^* | 5d \rangle = 0.9963,$$

and

$$\langle 6s_{(4f)}^* | 6s \rangle = 0.9991.$$

These overlap effects will be neglected in our calculation. The Hartree-Fock single-particle energies were found to be -0.4526 a.u. for the $5d_{(5p)}^*$ orbital and -0.5099 a.u. for the $5d_{(4f)}^*$ orbital. We recall that the single-particle energy of the $5d$ orbital is -0.4464 a.u., which was shown in Table II.

There was a noticeable discrepancy between the $5p$ ζ parameter that we obtained using nonrelativistic orbitals and the $5p$ ζ parameter that we obtained from orbitals which incorporated relativistic corrections. The $5p$ ζ parameter that we obtained from the MCHF77 code was $\zeta(5p) = 0.1699$ a.u., while the $5p$ ζ parameter that we obtained from the RCN35 code of Cowan and Griffin [26] operated in relativistic mode was $\zeta(5p) = 0.2292$ a.u. A fact that is pointed out by Cowan [27] and also in Ref. [26] is that the Blume-Watson technique [9] of obtaining the ζ parameters is sensitive to the effects of relativistic corrections on the radial orbitals. By using the RCN35 code in relativistic mode, we introduce the Darwin and mass-velocity terms into the nonrelativistic Hamiltonian [26]. The ζ parameters that we used in the calculation were obtained from the RCN35 code of Cowan and Griffin [26] operated in relativistic mode.

We used the MCDF [24] code in this portion of the calculation in order to determine the absolute energy shifts of the resonant states. The absolute shift will be contained within the variable $\Delta_R^{(\text{rel})}(J)$ in the manner present-

ed in Eq. (28):

$$D_R^{(1,\omega,J)} = E_G^{(0)} - E_R^{(0)} - E_R^{(1)} - \Delta_R(\omega) - \Delta_R^{(\text{rel})}(J) + \omega. \quad (38)$$

In order to obtain a value for the variable $\Delta_R^{(\text{rel})}(J)$, we performed a self-consistent-field calculation over the set of $(5p^6 5d^4)_{J=0}$ and $(5p^5 5d^5)_{J=1}$ states and a separate self-consistent-field calculation over the set of $(4f^{14} 5d^4)_{J=0}$ and $(4f^{13} 5d^5)_{J=1}$ states in tungsten using the MCDF code operated in "extended-average-level" [24] mode. We generated the lists of the oscillator strengths for the $5p^6 5d^4 \rightarrow 5p^5 5d^5$ transitions and the $4f^{14} 5d^4 \rightarrow 4f^{13} 5d^5$ transitions from the results of the MCDF [24] calculation. One set of oscillator strengths for the $5p^6 5d^4 \rightarrow 5p^5 5d^5$ transitions that we obtained from the MCDF [24] code is shown in bar-graph form in the lower portion of Fig. 8 and is labeled as "MCDF Babushkin gauge." The overall energy positions of these oscillator strengths are also those provided by the MCDF [24] code. In the nonrelativistic limit, the Babushkin gauge goes over into the length gauge [28]. The lists of the oscillator strengths that we obtained from the MCDF [24] code were compared with the oscillator strengths that we

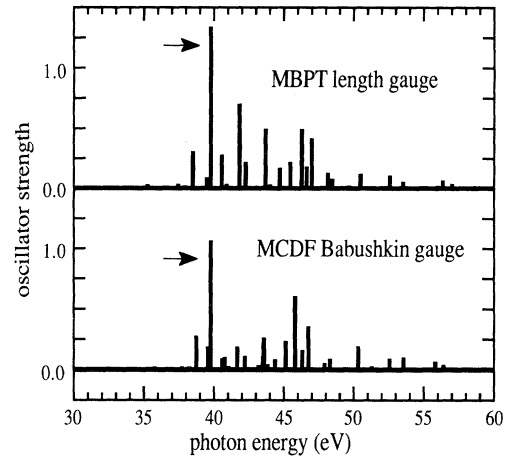


FIG. 8. Oscillator strengths and energy positions of the $5p^6 5d^4 \rightarrow 5p^5 5d^5$ transitions in tungsten. The lower portion of the figure shows the oscillator strengths that were obtained from a fully relativistic treatment (the MCDF [24] code) and the upper portion of the figure shows the oscillator strengths that were obtained from MBPT with spin-orbit mixed nonrelativistic orbitals. In the nonrelativistic limit, the Babushkin gauge goes over into the length gauge [28]. The overall energy positions of the oscillator strengths in the lower portion of the figure are those obtained from the MCDF [24] code. The energy *splittings* of the oscillator strengths in the upper portion of the figure are determined from the diagonalization of the total spin-orbit Hamiltonian $H = H_0 + H_C + H_{SO}$. This figure demonstrates how the overall relativistic energy shift $\Delta_R^{(\text{rel})}(J)$ was determined for the $5p^6 5d^4 \rightarrow 5p^5 5d^5$ transitions. We required that the energy eigenvalue of the first large peak in the oscillator strength distribution of our calculation should match the corresponding energy as provided by the MCDF [24] code. These peaks are indicated above by the arrows and occur at an energy of 1.4620 a.u. = 39.8 eV.

obtained from the eigenvectors of the diagonalized spin-orbit Hamiltonian $\langle H \rangle_{IJ}$ of Eq. (21). The corresponding set of oscillator strengths for the $5p^6 5d^4 \rightarrow 5p^5 5d^5$ transitions that we obtained using the spin-orbit mixed resonant states $|R^{(1)}(\text{RS})\rangle$ and our spin-orbit mixed initial state $|i\rangle$ from Eqs. (36a)–(36f) and (37) is shown in bar-graph form in the upper portion of Fig. 8 and is labeled as “MBPT length gauge.” The energy *splittings* of the MBPT oscillator strengths were those obtained from the energy eigenvalues $(E_R^{(0)} + E_R^{(1)})$ of Eq. (24). The qualitative structure and energy splittings of the oscillator strengths shown in Fig. 8 agree very well between the fully relativistic treatment (lower portion) and our approximate spin-orbit treatment (upper portion). The only large discrepancy appears to be the relative magnitude of some of the oscillator strengths in the 42–44 eV region. We mention that the sum of the MCDF [24] oscillator strengths shown here is 4.11, while the sum of the MBPT oscillator strengths shown here is 5.25. Because of the good qualitative agreement, it was possible to make a one-to-one correspondence between the large peaks that occurred in both lists. In order to determine the overall relativistic shift $\Delta_R^{(\text{rel})}(J)$ that we should include in our energy denominator $D_R^{(1,\omega,J)}$, we simply required that the absolute energy position of the first large peak in our calculation should match the absolute energy position of the same peak as given by the MCDF [24] code. The remaining energy positions in our calculation are determined by the diagonalization of the spin-orbit Hamiltonian as described in Sec. II B. For the $5p^6 5d^4 \rightarrow 5p^5 5d^5$ transitions, the reference peak in the oscillator strength distribution occurred at a photon energy of

$$1.4620 \text{ a.u.} = 39.8 \text{ eV}$$

and is the large peak indicated by the arrows in Fig. 8. For the $4f^{14} 5d^4 \rightarrow 4f^{13} 5d^5$ transitions, the reference peak in the oscillator strength distribution occurred at a photon energy of

$$0.9213 \text{ a.u.} = 25.1 \text{ eV} .$$

The complete identification and itemization of all of the resonant energies that were used in this calculation have been given by Boyle [17].

The transitions into the continuum that we include in this calculation are the $5d^4 \rightarrow 5d^3 kf$ and $5d^4 \rightarrow 5d^3 kp$ transitions. Due to the spin-orbit mixing of the resonant states $|R^{(1)}(\text{RS})\rangle$, there are 24 $J=1$ LSJ $5d^3 kf$ channels and 19 $J=1$ LSJ $5d^3 kp$ channels that are accessible from the $J=0$ initial state.

The total cross section including a generalized resonance calculation of the $5d$ partial cross section with respect to the intermediate-coupling initial state

$$|G(\text{GS})\rangle = |5d^4 [^5D, ^3P, ^3P, ^1S, ^1S]_{J=0}\rangle$$

is shown in Fig. 9. Aside from the corrections that are incorporated into the generalized resonance Eq. (29f), the MBPT corrections that have been included in this result involve all of the corrections that are discussed in Sec. III A for the nonresonant contributions, additional first-order ground-state correlation corrections to the $5d \rightarrow kf$

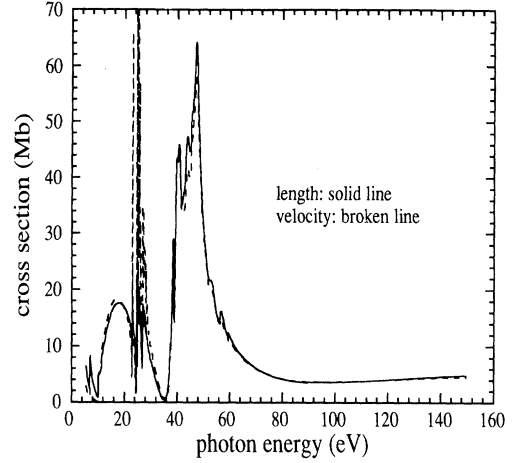


FIG. 9. The total resonant cross section in the length form (solid line) and the velocity form (dashed line) for the intermediate-coupling initial state $|G(\text{GS})\rangle = |5d^4 [^5D, ^3P, ^3P, ^1S, ^1S]_{J=0}\rangle$. The resonant transitions that are considered here are the $4f^{14} 5d^4 \rightarrow 4f^{13} 5d^5$ transitions (from 20 to 30 eV) and the $5p^6 5d^4 \rightarrow 5p^5 5d^5$ transitions (from 35 to 60 eV).

dipole matrix elements, and the first-order ground- and final-state correlation corrections to the $5p \rightarrow 5d_{(5p)}^*$ and $4f \rightarrow 5d_{(4f)}^*$ dipole matrix elements that are believed to be the most important with respect to all five initial states

$$|5d^4 [^5D, ^3P, ^3P, ^1S, ^1S]_{J=0}\rangle .$$

The additional ground-state correlation corrections that have been added to the $5d \rightarrow kf$ dipole matrix elements in Fig. 9 are Fig. 1(c) with

$$(n_a l_a, k_r l_r) = (5d, kf)$$

and

$$(n_b l_b, n_s l_s) = (5p, 5d_{(5p)}^*), (4f, 5d_{(4f)}^*) .$$

The ground-state correlation corrections that have been added to the $5p \rightarrow 5d_{(5p)}^*$ dipole matrix elements in Fig. 9 are Fig. 1(c) with

$$(n_a l_a, n_r l_r) = (5p, 5d_{(5p)}^*)$$

and

$$(n_b l_b, n_s l_s) = (5p, 5d_{(5p)}^*)$$

plus

$$(n_b l_b, k_s l_s) = (5d, kf) .$$

The ground-state correlation corrections that have been added to the $4f \rightarrow 5d_{(4f)}^*$ dipole matrix elements in Fig. 9 are Fig. 1(c) with

$$(n_a l_a, n_r l_r) = (4f, 5d_{(4f)}^*)$$

and

$$(n_b l_b, n_s l_s) = (4f, 5d_{(4f)}^*)$$

plus

$$(n_b l_b, k_s l_s) = (5d, kf) .$$

The final-state correlation corrections that have been added to the $5p \rightarrow 5d_{(5p)}^*$ dipole matrix elements in Fig. 9 are the principal-value portions of Fig. 1(b) with

$$(n_a l_a, n_r l_r) = (5p, 5d_{(5p)}^*)$$

and

$$(n_b l_b, k_s l_s) = (5d, kf) ,$$

and the final-state correlation corrections that have been added to the $4f \rightarrow 5d_{(4f)}^*$ dipole matrix elements in Fig. 9 are the principal-value portions of Fig. 1(b) with

$$(n_a l_a, n_r l_r) = (4f, 5d_{(4f)}^*)$$

and

$$(n_b l_b, k_s l_s) = (5d, kf) .$$

The exchange and potential correction versions of all the diagrams that are mentioned above have also been included.

In order to solve Eq. (29f) and obtain the $5d$ subshell contribution to Fig. 9, we inverted a 43×43 matrix for 1650 photon energy values between 10 and 150 eV. The dimensions of the matrix 43×43 result from the number of final LSJ channels that are considered: 24 $5d^3 kf$ channels plus 19 $5d^3 kp$ channels. We multiplied the inverted matrix against five sets of LSJ -coupled column vectors $T_I^{(0)} + \bar{T}_I^{(1, \omega, J)}$ [there is one column vector associated with each LSJ -coupled initial state that is itemized in Eq. (36)]. The resulting five sets of solution state column vectors T_M , according to Eq. (29f), were then weighted by the mixing coefficients $\alpha_m^{(i)}$ that are shown in Eq. (37).

An interesting aspect of the cross section that we would like to point out is the dip that occurs at approximately 35 eV. This dip does not appear in the non-resonant cross section that is shown in Fig. 7. In Fig. 9, we observe that the $4f^{14}5d^4 \rightarrow 4f^{13}5d^5$ resonant transitions introduce structure in the cross section from 20 to 30 eV, and the $5p^6 5d^4 \rightarrow 5p^5 5d^5$ resonant transitions introduce a large amount of oscillator strength into the $5d \rightarrow kl$ transitions from 35 to 60 eV. In the $5d$ partial cross section that is contained in Fig. 9, there are now approximately 9.5 units of oscillator strength, which is approximately 4.5 units of oscillator strength greater than the nonresonant $5d$ partial cross section shown in Fig. 5. The resonance structure in the calculated $5d$ partial cross section in the region of the $5p^6 5d^4 \rightarrow 5p^5 5d^5$ transitions can be described as two peaks separated by approximately 7 eV with the lower peak occurring at approximately 40 eV. There also appears to be a shoulder on the high-energy peak starting at approximately 43 eV. The dominance of two peaks in the resonance structure can be attributed to the spin-orbit splitting of the $5p$ subshell, and

the existence of the two distinct jj -coupled resonance channels $5p_{1/2} \rightarrow 5d_{3/2}$ and $5p_{3/2} \rightarrow 5d_{3/2}, 5d_{5/2}$.

In Fig. 10 we show the results of the $5d$ β asymmetry parameter according to Eqs. (30a)–(30e) for the intermediate-coupling initial state

$$|5d^4[{}^5D, {}^3P, {}^3P, {}^1S, {}^1S]_{J=0}\rangle$$

discussed above. The MBPT corrections that have been included in Fig. 10 are the same as the corrections that are discussed above for Fig. 9.

An expanded plot of the total cross section for the intermediate-coupling initial state

$$|5d^4[{}^5D, {}^3P, {}^3P, {}^1S, {}^1S]_{J=0}\rangle$$

is shown in Fig. 11 for the photon energy values ranging from 30 to 60 eV. Also shown in Fig. 11 are the experimental photoabsorption measurements of tungsten in the solid of Haensel *et al.* [6] (the triangles) and of tungsten in the atomic form of Costello *et al.* [8] (the circles). The solid-state data (triangles) are given in absolute units and the atomic data (circles) are given in relative units. The scale for the atomic data is given to the right of Fig. 11. The normalization of the atomic data was chosen so that the experimental results above 51 eV and below 32 eV would coincide roughly with our calculation. The photoabsorption measurements of tungsten in the solid that were performed by Weaver and Olson [7] and that were mentioned in the Introduction show good quantitative agreement with the solid-state measurements of Haensel *et al.* [6] displayed here (the triangles).

There are some qualitative similarities between our calculation and the photoabsorption measurements of tungsten in the solid (the triangles). These similarities in-

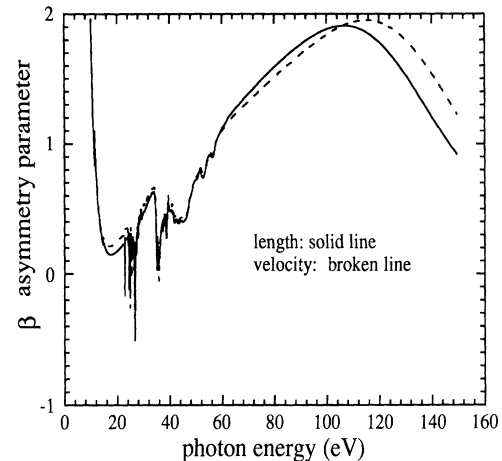


FIG. 10. The β asymmetry parameter for the $5d$ subshell of tungsten including resonant effects in the length form (solid line) and the velocity form (dashed line) for the intermediate-coupling initial state $|G(\text{GS})\rangle = |5d^4[{}^5D, {}^3P, {}^3P, {}^1S, {}^1S]_{J=0}\rangle$. The MBPT corrections on the $5d$ partial cross section that have been included in this figure are the same as those corrections that are included in Fig. 9.

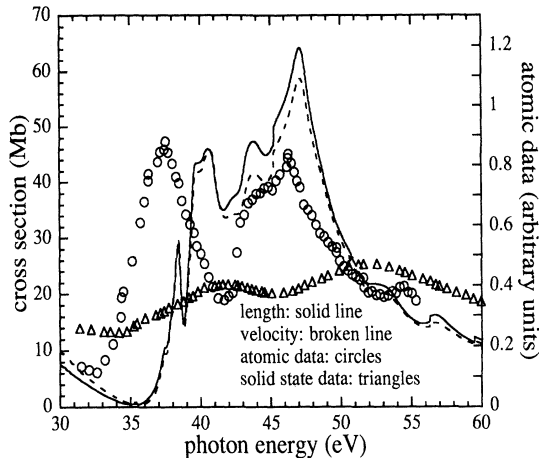


FIG. 11. The total resonant cross section in the length form (solid line) and the velocity form (dashed line) for the intermediate-coupling initial state $|G(GS)\rangle = |5d^4[{}^5D, {}^3P, {}^3P, {}^1S, {}^1S]_{J=0}\rangle$ for photon energies from 30 to 60 eV. The circles represent the atomic data of Costello *et al.* [8] and the triangles represent the solid-state data of Haensel *et al.* [6].

clude the existence of two dominant peaks. However, these peaks do not have the prominence of our calculation or of the atomic measurements. The second peak in the solid-state data also occurs at a slightly higher energy than either our calculation or the atomic measurement.

In Fig. 11 we can see more qualitative similarities between our calculation and the photoabsorption measurements of tungsten in the atomic state (the circles). These similarities include the extreme dip that occurs at ≈ 34 eV and the two dominant peaks that are separated by ≈ 8 eV, as well as the shoulder on the high-energy peak occurring at ≈ 43 eV and the rapid drop-off of this peak beginning at 46.3 eV and continuing to ≈ 50 eV. However, the main disagreement between the two results occurs in the overall position of the first peak with respect to the second peak and its overall magnitude with respect to the second peak.

IV. CONCLUSIONS

A photoionization cross-section calculation of atomic tungsten has been performed for photon energies ranging from the ionization threshold of tungsten to 150 eV and considering excitations from the $4f$, $5s$, $5p$, $5d$, and $6s$ subshells. The effects of the strong $5p^6 5d^4 \rightarrow 5p^5 5d^5$ and $4f^{14} 5d^4 \rightarrow 4f^{13} 5d^5$ transitions have been included as resonant contributions to the $5d$ partial cross section from the intermediate-coupling initial state

$$|5d^4[{}^5D, {}^3P, {}^3P, {}^1S, {}^1S]_{J=0}\rangle.$$

In the energy range that we considered, the $5d^4 \rightarrow 5d^3kl$ photoionization transitions dominated the total cross section. Additionally, we observed a significant dependence on the $5p^6 5d^4 \rightarrow 5p^5 5d^5$ transitions.

One of the purposes of this work was to take a complex open-shell atom and obtain a photoionization cross section for this atom with a minimum of computer time. In the case of the $J=0$ to 1 transitions in atomic tungsten, the linear system of equations that had to be solved for was contained in a 43×43 matrix. Using the techniques that are described in this paper on an arbitrary atom, one would invert a matrix whose dimensions would be the number of final LSJ channels that are considered. A comparable calculation that uses our coupled-integral-equations technique [29] would involve solving a linear system of equations similar in form to Eq. (29f). However, the size of the linear system for the $J=0$ to 1 transitions in tungsten would have been roughly two orders of magnitude larger than the size of the linear system that we solved in this work (1884×1884 versus 43×43). Since we would have been inverting the matrix mentioned above for 1650 photon energy values, the techniques that are discussed in this work correspond to a substantial savings of computer time. Moreover, by including the real ω -dependent energy shift of Eqs. (26) and (27), we have approximated, to first order, the type of coupled-equations calculation that is mentioned above [29,17].

When we compare our calculated results with the experimental results, the main discrepancy is the absence of a strong transition in our calculation that occurs at ≈ 37 eV consistent with the data of Costello *et al.* [8]. Above ≈ 43 eV, we can reproduce the qualitative nature of the atomic measurements fairly well using the spin-orbit mixed initial state

$$|5d^4[{}^5D, {}^3P, {}^3P, {}^1S, {}^1S]_{J=0}\rangle.$$

The fact that we reproduce, in a general way, the structure occurring above 43 eV in the atomic data signifies that the $J=0$ to 1 transitions are being observed in the experimental measurements of Costello *et al.* [8]. It is unclear to us, however, what type of transitions are producing the strong peak in the absorption spectrum at 37 eV.

In order to account for the discrepancy between our calculation and the atomic measurements, it was suggested that some of the tungsten atoms in the laser-ablation experiment might have been initially prepared in higher-lying J levels within the $(5d^4)^5D_J$ coupling [8,17,30]. According to Moore's [31] table of atomic energy levels, all of the LSJ terms of tungsten with the couplings $5d^4[{}^5D_{J=0,1,2,3,4}]$ are within 0.77 eV of each other. This possibility was investigated by Boyle [17], who calculated a generalized resonance cross section, according to Eq. (29f), for each of the J values of the initial state $(5d^4)^5D_J$ ranging from $J=0$ to 4. The resulting cross sections were then summed together according to their statistical weight $(2J+1)$. According to this averaging procedure, the $J=0$ to 1 transitions would be weighted the least ($\frac{1}{25}$), while the $J=4$ to 3-5 transitions would be weighted the most ($\frac{9}{25}$). The resulting cross section does not display the hoped-for peak at 37 eV, however. The general effect obtained in the calculation of Boyle [17] was a reduction and broadening of the two dominant peaks. It is interesting to point out, however, that the positions of

the two peaks in the calculation of Boyle [17] coincide with the positions of the peaks obtained in the solid-state measurements of Haensel *et al.* [6] and the solid-state measurements of Weaver and Olson [7]. That is, the two peaks in the statistically weighted calculation by Boyle [17] $(2J+1)(5d^4)^5 D_J$ become separated by ≈ 12 eV and are shifted in energy so that the higher-energy peak occurs at ≈ 53 eV.

There is also the possibility that other configurations might be present in the atomic sample under investigation [8]. According to Moore's [31] table of atomic energy levels, the $[5d^5(^6S)6s]^7S_{J=3}$ state lies 0.366 eV above the $5d^4[^5D_{J=0}]$ state. Also, according to the Thomas-Reiche-Kuhn sum rule [25], the $5d^56s$ initial state would contain one more unit of oscillator strength for transitions from the $n=5$ level than the $5d^46s^2$ initial state. However, we did not investigate the possibility of this in our paper.

We hope that the availability of the measurements of Costello *et al.* [8] and our calculation will stimulate further investigations over this energy region. In closing, we feel that the techniques that are discussed in this paper will be useful when performing calculations on complex, open-shell atoms and should be able to provide meaningful results with comparative ease.

ACKNOWLEDGMENTS

We would like to acknowledge useful discussions of this problem with Dr. M. Kutzner and Dr. J. W. Cooper, and valuable assistance in utilizing the MCDF code from Dr. V. Radojevic. We would also like to thank Dr. E. Kennedy for communicating experimental measurements to us prior to their publication, and Dr. R. Cowan for allowing us access to the RCN35 and RCG10 computer codes. This work was supported by a grant from the U.S. National Science Foundation and by a computing grant from the University of Virginia.

APPENDIX A

In this Appendix we derive the form of the dipole operator in the velocity gauge that is presented in Eq. (7). We begin by reviewing different forms of the radial operator that have been used in nonrelativistic calculations. Using Eqs. (1b) and (1c), we define a nonrelativistic Hamiltonian

$$H_{\text{NR}} = H_0 + H_C, \quad (\text{A1a})$$

with

$$H_0 = \sum_{i=1}^N \left[-\frac{\nabla_i^2}{2} - \frac{Z}{r_i} + V_i \right] = \sum_{i=1}^N h_i \quad (\text{A1b})$$

and

$$H_C = \sum_{\substack{i,j=1 \\ (i < j)}}^N \frac{1}{r_{ij}} - \sum_{i=1}^N V_i. \quad (\text{A1c})$$

For matrix elements of exact solutions to the nonrelativistic Hamiltonian H_{NR} , we can itemize the following

forms of the radial operator \mathbf{R}_{op} [21]:

$$\langle \Psi_f^{\text{NR}} | \mathbf{R}_{\text{op}} | \Psi_0^{\text{NR}} \rangle = \left\langle \Psi_f^{\text{NR}} \left| \sum_j \mathbf{r}_j \right| \Psi_0^{\text{NR}} \right\rangle, \quad (\text{A2a})$$

$$\langle \Psi_f^{\text{NR}} | \mathbf{R}_{\text{op}} | \Psi_0^{\text{NR}} \rangle = \frac{-i}{(E_f^{\text{NR}} - E_0^{\text{NR}})} \left\langle \Psi_f^{\text{NR}} \left| \sum_j \mathbf{p}_j \right| \Psi_0^{\text{NR}} \right\rangle, \quad (\text{A2b})$$

and

$$\langle \Psi_f^{\text{NR}} | \mathbf{R}_{\text{op}} | \Psi_0^{\text{NR}} \rangle = \frac{1}{(E_f^{\text{NR}} - E_0^{\text{NR}})^2} \left\langle \Psi_f^{\text{NR}} \left| \sum_j \frac{\partial}{\partial r_j} \left[\frac{-Z}{r_j} \right] \hat{\mathbf{r}}_j \right| \Psi_0^{\text{NR}} \right\rangle. \quad (\text{A2c})$$

In the equations that are shown above, the variables E_f^{NR} and E_0^{NR} are the exact energy eigenvalues of the wave functions Ψ_f^{NR} and Ψ_0^{NR} with respect to the nonrelativistic Hamiltonian H_{NR} . The expression that is presented in Eq. (A2a) defines the length form of the radial matrix element, the expression that is presented in Eq. (A2b) defines the velocity form of the radial matrix element, and the expression that is presented in Eq. (A2c) defines the acceleration form of the radial matrix element.

We consider the introduction of the spin-orbit interaction H_{SO} into the Hamiltonian that is shown in Eq. (A1a). Rather than using the form of the spin-orbit interaction that is shown in Eq. (1d), we will write the spin-orbit operator as [32]

$$H_{\text{SO}} = \frac{1}{2c^2} \sum_{i=1}^N \frac{1}{r_i} \frac{\partial V_i}{\partial r_i} \mathbf{l}_i \cdot \mathbf{s}_i. \quad (\text{A3a})$$

The variable V_i in Eq. (A3a) represents the approximate central potential of electron i due to the nucleus and the other electrons. Because we are concerned primarily with order-of-magnitude estimates in this appendix, we will approximate V_i as a local central potential with a screened nuclear charge Z^* :

$$\begin{aligned} O & \left\langle \Psi_f^{\text{NR}} \left| \frac{\partial V_i}{\partial r_i} \hat{\mathbf{r}}_i \right| \Psi_0^{\text{NR}} \right\rangle \\ & = O \left\langle \Psi_f^{\text{NR}} \left| \frac{\partial}{\partial r_i} \left[\frac{-Z^*}{r_i} \right] \hat{\mathbf{r}}_i \right| \Psi_0^{\text{NR}} \right\rangle. \end{aligned} \quad (\text{A3b})$$

As pointed out by Huang and Starace [33], the coupling with an electromagnetic field in the length gauge remains unchanged from the nonrelativistic form in the presence of the spin-orbit interaction:

$$\langle \Psi_f | \mathbf{R}_{\text{op}} | \Psi_0 \rangle = \left\langle \Psi_f \left| \sum_j \mathbf{r}_j \right| \Psi_0 \right\rangle. \quad (\text{A4})$$

In the equation shown above, Ψ_0 and Ψ_f are now the exact eigenfunctions of the total spin-orbit Hamiltonian $H_{\text{NR}} + H_{\text{SO}}$. In order to construct the velocity form of the radial operator, we evaluate the commutator of the radial operator and the Hamiltonian of Eq. (1a):

$$\begin{aligned}
& \left\langle \Psi_f \left| \left[\sum_j \mathbf{r}_j, H_{\text{NR}} + H_{\text{SO}} \right] \right| \Psi_0 \right\rangle \\
&= i \left\langle \Psi_f \left| \sum_j \mathbf{p}_j \right| \Psi_0 \right\rangle \\
&+ \left\langle \Psi_f \left| \frac{1}{2c^2} \sum_j \frac{\partial V_j}{\partial r_j} \frac{[\mathbf{r}_j, l_j \cdot \mathbf{s}_j]}{r_j} \right| \Psi_0 \right\rangle. \quad (\text{A5a})
\end{aligned}$$

Equation (A5a) can be rewritten as

$$\begin{aligned}
\langle \Psi_f | \mathbf{R}_{\text{op}} | \Psi_0 \rangle &= \frac{-i}{(E_f - E_0)} \left\langle \Psi_f \left| \sum_j \mathbf{p}_j \right| \Psi_0 \right\rangle \\
&+ \frac{1}{(8)^{1/2} c^2 (E_f - E_0)} \\
&\times \left\langle \Psi_f \left| \sum_j \frac{\partial V_j}{\partial r_j} \hat{\mathbf{R}}_j^{(\text{SO})} \right| \Psi_0 \right\rangle, \quad (\text{A5b})
\end{aligned}$$

with

$$\begin{aligned}
\hat{\mathbf{R}}^{(\text{SO})} &= \frac{\hat{\mathbf{x}} - i\hat{\mathbf{y}}}{2} \begin{bmatrix} -C_1^1 & -\sqrt{2}C_0^1 \\ 0 & C_1^1 \end{bmatrix} \\
&+ \frac{\hat{\mathbf{x}} + i\hat{\mathbf{y}}}{2} \begin{bmatrix} -C_{-1}^1 & 0 \\ \sqrt{2}C_0^1 & C_{-1}^1 \end{bmatrix} + \hat{\mathbf{z}} \begin{bmatrix} 0 & C_{-1}^1 \\ C_1^1 & 0 \end{bmatrix}. \quad (\text{A5c})
\end{aligned}$$

In Eq. (A5b), the variables E_f and E_0 are the eigenvalues of the total spin-orbit Hamiltonian with respect to the eigenfunctions Ψ_f and Ψ_0 . In Eq. (A5c), the matrices correspond to two-component spinor operators, and the variables C_m^l are spherical tensor operators [16]. In terms of the radial unit vector

$$\hat{\mathbf{r}} = \frac{\hat{\mathbf{x}} - i\hat{\mathbf{y}}}{(2)^{1/2}} (-C_1^1) + \frac{\hat{\mathbf{x}} + i\hat{\mathbf{y}}}{(2)^{1/2}} (C_{-1}^1) + \hat{\mathbf{z}} (C_0^1), \quad (\text{A6a})$$

we have the identity

$$\hat{\mathbf{R}}^{(\text{SO})\dagger} \cdot \hat{\mathbf{R}}^{(\text{SO})} = \hat{\mathbf{r}}^\dagger \cdot \hat{\mathbf{r}} = 1. \quad (\text{A6b})$$

Therefore, in an order-of-magnitude sense, we would expect the following relationship to hold:

$$\begin{aligned}
O(\langle l' m'_l \frac{1}{2} m'_s | \hat{\mathbf{R}}^{(\text{SO})} | l m_l, \frac{1}{2} m_s \rangle) \\
= O(\langle l' m'_l \frac{1}{2} m'_s | \hat{\mathbf{r}} | l m_l, \frac{1}{2} m_s \rangle). \quad (\text{A6c})
\end{aligned}$$

Next, we consider the radial integrals that are needed in order to evaluate the second term on the right-hand side of Eq. (A5b). We will make use of the approximation that is given in Eq. (A3b), which involves replacing the potential V_j with a screened nuclear charge. With this substitution, Eq. (A5b) becomes

$$\langle \Psi_f | \hat{\mathbf{R}}_{\text{op}} | \Psi_0 \rangle = \frac{-i}{(E_f - E_0)} \left\langle \Psi_f \left| \sum_j \hat{\mathbf{p}}_j \right| \Psi_0 \right\rangle + \frac{1}{(8)^{1/2} c^2 (E_f - E_0)} O \left[\left\langle \Psi_f \left| \sum_j \frac{\partial}{\partial r_j} \left[\frac{-Z^*}{r_j} \right] \hat{\mathbf{R}}_j^{(\text{SO})} \right| \Psi_0 \right\rangle \right]. \quad (\text{A7})$$

We wish to relate the second term on the right-hand side of Eq. (A7) to the acceleration form of the radial matrix element that is given in Eq. (A2c). In order to accomplish this, we make the assumption that the exact radial matrix element with the spin-orbit interaction in the full Hamiltonian is roughly equivalent to its nonrelativistic counterpart in the acceleration gauge,

$$\begin{aligned}
O \left[\langle \Psi_f | \mathbf{R}_{\text{op}} | \Psi_0 \rangle \right] \\
= \frac{1}{(E_f^{\text{NR}} - E_0^{\text{NR}})^2} \\
\times O \left[\left\langle \Psi_f^{\text{NR}} \left| \sum_j \frac{\partial}{\partial r_j} \left[\frac{-Z}{r_j} \right] \hat{\mathbf{r}}_j \right| \Psi_0^{\text{NR}} \right\rangle \right]. \quad (\text{A8a})
\end{aligned}$$

Furthermore, we assume that if we change the wave functions and eigenvalues used on the right-hand side of Eq. (A8a) to exact solutions of the spin-orbit Hamiltonian, then we remain within this order-of-magnitude estimate, or

$$\begin{aligned}
O \left[\langle \Psi_f | \mathbf{R}_{\text{op}} | \Psi_0 \rangle \right] \\
= \frac{1}{(E_f - E_0)^2} O \left[\left\langle \Psi_f \left| \sum_j \frac{\partial}{\partial r_j} \left[\frac{-Z}{r_j} \right] \hat{\mathbf{r}}_j \right| \Psi_0 \right\rangle \right]. \quad (\text{A8b})
\end{aligned}$$

Finally, if we replace Z in Eq. (A8b) by its screened counterpart Z^* and use Eq. (A6c), we obtain

$$\begin{aligned}
O \left[\langle \Psi_f | \mathbf{R}_{\text{op}} | \Psi_0 \rangle \right] \\
= \frac{1}{(E_f - E_0)^2} O \left[\left\langle \Psi_f \left| \sum_j \frac{\partial}{\partial r_j} \left[\frac{-Z^*}{r_j} \right] \hat{\mathbf{R}}_j^{(\text{SO})} \right| \Psi_0 \right\rangle \right]. \quad (\text{A8c})
\end{aligned}$$

Therefore, Eq. (A7) can be written as

$$\begin{aligned}
\langle \Psi_f | \hat{\mathbf{R}}_{\text{op}} | \Psi_0 \rangle &= \frac{-i}{(E_f - E_0)} \left\langle \Psi_f \left| \sum_j \mathbf{p}_j \right| \Psi_0 \right\rangle \\
&+ \frac{(E_f - E_0)}{(8)^{1/2} c^2} O \left[\langle \Psi_f | \mathbf{R}_{\text{op}} | \Psi_0 \rangle \right], \quad (\text{A9})
\end{aligned}$$

or

$$\langle \Psi_f | \mathbf{R}_{\text{op}} | \Psi_0 \rangle = \frac{-i}{(E_f - E_0)} \left\langle \Psi_f \left| \sum_j \mathbf{p}_j \right| \Psi_0 \right\rangle + O \left[\frac{E_f - E_0}{c^2} \right]. \quad (\text{A10})$$

Notice that, due to the magnitude of the speed-of-light factor c^2 in relation to the photon energies $\omega = E_f - E_0$ in Eq. (A9), the assumptions made in Eqs. (A3b) and (A8a)–(A8c) could vary by a factor of 10 but the terms involving the commutator with the spin-orbit interaction would still be sufficiently damped as to be negligible in our work.

APPENDIX B

In this appendix we derive Eq. (35a). This equation determines the form of the weighting factor $(\lambda_t)^2$ for the

cross section when we use a jj -coupled multiconfiguration initial state and a jj -coupled multiconfiguration ionic core.

Using the notation that is introduced in Eq. (32), we have

$$|i\rangle = \alpha_1^{(i)} |1\rangle + \alpha_2^{(i)} |2\rangle + \alpha_3^{(i)} |3\rangle, \quad (\text{B1a})$$

with

$$|1\rangle = |(5d_{3/2}^4) J=0, M_J=0\rangle, \quad (\text{B1b})$$

$$|2\rangle = |((5d_{3/2}^2) J=0; (5d_{5/2}^2) J=0) J=0, M_J=0\rangle, \quad (\text{B1c})$$

and

$$|3\rangle = |((5d_{3/2}^2) J=2; (5d_{5/2}^2) J=2) J=0, M_J=0\rangle. \quad (\text{B1d})$$

Using the notation that is introduced in Eq. (34), we have

$$|f^{(t)}\rangle = \beta_{t1} |f_1\rangle + \beta_{t2} |f_2\rangle + \sum_{s=3}^{N_s} \beta_{ts} |f_s\rangle, \quad (\text{B2a})$$

with

$$|f_1\rangle = |(((nl_j^{2j}) J=j; (5d_{3/2}^4) J=j; (kj_r) J=j_r) J=1, M_J=0)\rangle, \quad (\text{B2b})$$

$$|f_2\rangle = |(((nl_j^{2j}) J=j; (5d_{3/2}^2) J=0) J=j; (5d_{5/2}^2) J=0) J=j; (kj_r) J=j_r) J=1, M_J=0\rangle, \quad (\text{B2c})$$

and

$$|f_s\rangle_{(s \geq 3)} = |(((nl_j^{2j}) J=j; (5d_{3/2}^2) J=2) J=j_s; (5d_{5/2}^2) J=2) J=j; (kj_r) J=j_r) J=1, M_J=0\rangle. \quad (\text{B2d})$$

It is easy to see that

$$\begin{aligned} \langle f_1 | C_0^1 | 1 \rangle &= \langle f_2 | C_0^1 | 2 \rangle \\ &= \langle ((nl_j^{2j}) J=j; (kj_r) J=j_r) J=1, M_J=0 | C_0^1 | (nl_j^{2j+1}) J=0, M_J=0 \rangle. \end{aligned} \quad (\text{B3})$$

In Eq. (B3), we have used C_0^1 as the spherical tensor operator appropriate to the dipole interaction [16]. In this formula we are concerned primarily with the angular dependence of the dipole matrix elements. We rewrite the state $|3\rangle$ as

$$|3\rangle = \sum_{m_2, m_4} \langle j_2=2, m_2; j_4=2, m_4 | j=0, m=0 \rangle | (nl_j^{2j+1}) j_1=0, m_1=0 \rangle | (5d_{3/2}^2) j_2=2, m_2 \rangle | (5d_{5/2}^2) j_4=2, m_4 \rangle. \quad (\text{B4})$$

In Eq. (B4) the $\langle j_1 m_1; j_2 m_2 | jm \rangle$ are Clebsch-Gordan coefficients. In terms of $3j$ symbols, we can write [34]

$$\begin{bmatrix} j_1 & j_2 & j \\ m_1 & m_2 & -m \end{bmatrix} = (-1)^{j_1 - j_2 + m} (2j+1)^{-1/2} \langle j_1 m_1; j_2 m_2 | jm \rangle. \quad (\text{B5a})$$

If we use the identity [34]

$$\begin{bmatrix} j & j & 0 \\ m_1 & m_2 & 0 \end{bmatrix} = (-1)^{j-m_1} (2j+1)^{-1/2} \delta(m_1, -m_2), \quad (\text{B5b})$$

then Eq. (B4) can be rewritten as

$$|3\rangle = \sum_{m_2, m_4} (5)^{-1/2} (-1)^{-m_2} \delta(m_2, -m_4) | (nl_j^{2j+1}) j_1=0, m_1=0 \rangle | (5d_{3/2}^2) j_2=2, m_2 \rangle | (5d_{5/2}^2) j_4=2, m_4 \rangle. \quad (\text{B6})$$

Likewise, we will have

$$\begin{aligned} |f_s\rangle &= \sum_{\substack{m_5, m_6, m_7, \\ m_8, m_9, m_{10}}} \langle j, m_5; j_6=2, m_6 | j_s, m_7 \rangle \langle j_s, m_7; j_8=2, m_8 | j, m_9 \rangle \langle j, m_9; j_r, m_{10} | j_{11}=1, m_{11}=0 \rangle \\ &\quad \times | (nl_j^{2j}) j, m_5 \rangle | (5d_{3/2}^2) j_6=2, m_6 \rangle | (5d_{5/2}^2) j_8=2, m_8 \rangle | (kj_r) j_r, m_{10} \rangle. \end{aligned} \quad (\text{B7a})$$

In terms of 3j symbols, Eq. (B7a) can be rewritten as

$$|f_s\rangle = \sum_{\substack{m_5, m_6, m_7, \\ m_8, m_9, m_{10}}} (-1)^{2j+j_s-j_r+m_7+m_9} \sqrt{3(2j_s+1)(2j+1)} \begin{Bmatrix} j & 2 & j_s \\ m_5 & m_6 & -m_7 \end{Bmatrix} \begin{Bmatrix} j_s & 2 & j \\ m_7 & m_8 & -m_9 \end{Bmatrix} \begin{Bmatrix} j & j_r & 1 \\ m_9 & m_{10} & 0 \end{Bmatrix} \\ \times \langle (nl_j^{2j})j, m_5 \rangle \langle (5d_{3/2}^2)j_6=2, m_6 \rangle \langle (5d_{5/2}^2)j_8=2, m_8 \rangle \langle (kj_r)j_r, m_{10} \rangle . \quad (\text{B7b})$$

Using Eqs. (B6) and (B7b), we obtain

$$\langle f_s | C_0^1 | 3 \rangle = \sum_{\substack{m_2, m_4, m_5, m_6, \\ m_7, m_8, m_9, m_{10}}} \langle (5d_{3/2}^2)j_6=2, m_6 \rangle \langle (5d_{3/2}^2)j_2=2, m_2 \rangle \langle (5d_{5/2}^2)j_8=2, m_8 \rangle \langle (5d_{5/2}^2)j_4=2, m_4 \rangle \\ \times \langle (nl_j^{2j})j, m_5; (kj_r)j_r, m_{10} | C_0^1 | (nl_j^{2j+1})j_1=0, m_1=0 \rangle \\ \times (-1)^{2j+j_s-j_r+m_7+m_9-m_2} \delta(m_2, -m_4) (5)^{-1/2} \sqrt{3(2j_s+1)(2j+1)} \\ \times \begin{Bmatrix} j & 2 & j_s \\ m_5 & m_6 & -m_7 \end{Bmatrix} \begin{Bmatrix} j_s & 2 & j \\ m_7 & m_8 & -m_9 \end{Bmatrix} \begin{Bmatrix} j & j_r & 1 \\ m_9 & m_{10} & 0 \end{Bmatrix} . \quad (\text{B8})$$

Since

$$\langle (5d_{3/2}^2)j_6=2, m_6 | (5d_{3/2}^2)j_2=2, m_2 \rangle = \delta(m_6, m_2) , \quad (\text{B9a})$$

$$\langle (5d_{5/2}^2)j_8=2, m_8 | (5d_{5/2}^2)j_4=2, m_4 \rangle = \delta(m_8, m_4) , \quad (\text{B9b})$$

and also using $\delta(m_2, -m_4)$, Eq. (B8) can be written as

$$\langle f_s | C_0^1 | 3 \rangle = \sum_{\substack{m_2, m_5, \\ m_7, m_9, m_{10}}} (-1)^{2j+j_s-j_r+m_7+m_9-m_2} (5)^{-1/2} \sqrt{3(2j_s+1)(2j+1)} \\ \times \langle (nl_j^{2j})j, m_5; (kj_r)j_r, m_{10} | C_0^1 | (nl_j^{2j+1})j_1=0, m_1=0 \rangle \\ \times \begin{Bmatrix} j & 2 & j_s \\ m_5 & m_2 & -m_7 \end{Bmatrix} \begin{Bmatrix} j_s & 2 & j \\ m_7 & -m_2 & -m_9 \end{Bmatrix} \begin{Bmatrix} j & j_r & 1 \\ m_9 & m_{10} & 0 \end{Bmatrix} . \quad (\text{B10})$$

Using the fact that $m_5+m_2-m_7=0$ from the first 3j symbol which appears in Eq. (B10), we obtain $(-1)^{m_7-m_2}=(-1)^{m_5}$. We also use the relation [34]

$$\sum_{m_2, m_7} \begin{Bmatrix} j & 2 & j_s \\ m_5 & m_2 & -m_7 \end{Bmatrix} \begin{Bmatrix} j_s & 2 & j \\ m_7 & -m_2 & -m_9 \end{Bmatrix} = \frac{\delta(m_9, m_5)}{(2j+1)} \quad (\text{B11})$$

and the fact that $j+m_9$ must equal an integer to obtain

$$\langle f_s | C_0^1 | 3 \rangle = \sum_{m_9, m_{10}} (-1)^{j_s-j_r} \left[\frac{3(2j_s+1)}{5(2j+1)} \right]^{1/2} \begin{Bmatrix} j & j_r & 1 \\ m_9 & m_{10} & 0 \end{Bmatrix} \langle (nl_j^{2j})j, m_9; (kj_r)j_r, m_{10} | C_0^1 | (nl_j^{2j+1})j_1=0, m_1=0 \rangle . \quad (\text{B12})$$

Using Eq. (B5a) we obtain

$$\langle f_s | C_0^1 | 3 \rangle = \sum_{m_9, m_{10}} (-1)^{j_s-j} \left[\frac{2j_s+1}{5(2j+1)} \right]^{1/2} \langle j, m_9; j_r, m_{10} | j_{11}=1, m_{11}=0 \rangle \\ \times \langle (nl_j^{2j})j, m_9; (kj_r)j_r, m_{10} | C_0^1 | (nl_j^{2j+1})j_1=0, m_1=0 \rangle . \quad (\text{B13a})$$

Finally, using Eq. (B3), we obtain

$$\langle f_s | C_0^1 | 3 \rangle = (-1)^{j_s-j} \left[\frac{2j_s+1}{5(2j+1)} \right]^{1/2} \langle ((nl_j^{2j})j; (kj_r)j_r)j_{11}=1, m_{11}=0 | C_0^1 | (nl_j^{2j+1})j_1=0, m_1=0 \rangle , \quad (\text{B13b})$$

$$= (-1)^{j_s - j} \left[\frac{2j_s + 1}{5(2j + 1)} \right]^{1/2} \langle f_1 | C_0^1 | 1 \rangle . \quad (\text{B13c})$$

Therefore, we obtain the final form of Eq. (35a), using Eqs. (B1)–(B3) and (B13c):

$$\langle f^{(t)} | C_0^1 | i \rangle = \langle f_1 | C_0^1 | 1 \rangle \left[\beta_{t1} \alpha_1^{(i)} + \beta_{t2} \alpha_2^{(i)} + \sum_{s=3}^{N_s} \beta_{ts} \alpha_s^{(i)} (-1)^{j - j_s} \left[\frac{2j_s + 1}{5(2j + 1)} \right]^{1/2} \right] , \quad (\text{B14a})$$

$$= \langle f_1 | C_0^1 | 1 \rangle \lambda_t . \quad (\text{B14b})$$

-
- [1] H. P. Kelly, Phys. Rev. **182**, 84 (1969).
 [2] Z. Qian, S. L. Carter, and H. P. Kelly, Phys. Rev. A **33**, 1751 (1986).
 [3] W. Wijesundera and H. P. Kelly, Phys. Rev. A **36**, 3187 (1987).
 [4] Z. Altun, J. Phys. B **25**, 2279 (1992).
 [5] L. J. Garvin, Ph.D. thesis, University of Virginia, 1983, pp. 128–150 (unpublished).
 [6] R. Haensel, K. Radler, B. Sonntag, and C. Kunz, Solid State Commun. **7**, 1495 (1969).
 [7] J. H. Weaver and C. G. Olson, Phys. Rev. B **14**, 3251 (1976).
 [8] J. T. Costello, E. T. Kennedy, B. F. Sonntag, and C. L. Cromer, J. Phys. B **24**, 5063 (1991).
 [9] M. Blume and R. E. Watson, Proc. R. Soc. London, Ser. A **270**, 127 (1962).
 [10] U. Fano and J. W. Cooper, Rev. Mod. Phys. **40**, 441 (1968).
 [11] H. P. Kelly and A. Ron, Phys. Rev. A **5**, 168 (1972).
 [12] H. P. Kelly, Phys. Rev. **136**, B896 (1964); S. L. Carter, Ph.D. thesis, University of Virginia, 1976, pp. 93–115 (unpublished).
 [13] K. A. Brueckner, Phys. Rev. **100**, 36 (1955).
 [14] J. Goldstone, Proc. R. Soc. London, Ser. A **239**, 267 (1957).
 [15] H. P. Kelly, in *Advances in Theoretical Physics*, edited by Keith A. Brueckner (Academic, New York, 1968), Vol. 2, pp. 75–169; *Advances in Chemical Physics*, edited by R. Lefebvre and C. Moser (Interscience, London, 1969), Vol. 14, pp. 129–190.
 [16] I. Lindgren and J. Morrison, *Atomic Many-Body Theory*, 2nd ed. (Springer-Verlag, Berlin, 1986).
 [17] J. J. Boyle, Ph.D. thesis, University of Virginia, 1992 (unpublished).
 [18] L. M. Frantz, R. L. Mills, R. G. Newton, and A. M. Sessler, Phys. Rev. Lett. **1**, 340 (1958); B. A. Lippmann, M. H. Mittleman, and K. M. Watson, Phys. Rev. **116**, 920 (1959); R. T. Pu and E. S. Chang, *ibid.* **151**, 31 (1966); H. J. Silverstone and M. L. Yin, J. Chem. Phys. **49**, 2026 (1968); S. Huzinaga and C. Arnau, Phys. Rev. A **1**, 1285 (1970).
 [19] A. W. Fliflet and H. P. Kelly, Phys. Rev. A **10**, 508 (1974).
 [20] G. Wendin, J. Phys. B **3**, 455 (1970); **3**, 466 (1970).
 [21] A. F. Starace, in *Encyclopedia of Physics*, edited by W. Mehlhorn (Springer-Verlag, Berlin, 1982), Vol. 31, pp. 1–121.
 [22] L. D. Landau and E. M. Lifshitz, *Quantum Mechanics (Non-Relativistic Theory)*, 3rd ed. (Pergamon, Oxford, 1977), pp. 566–567.
 [23] C. Froese Fischer, Comput. Phys. Commun. **14**, 145 (1978).
 [24] I. P. Grant, B. J. McKenzie, P. H. Norrington, D. F. Mayers, and N. C. Pyper, Comput. Phys. Commun. **21**, 207 (1980).
 [25] H. A. Bethe and E. E. Salpeter, *Quantum Mechanics of One- and Two-Electron Atoms* (Plenum, New York, 1977), p. 256.
 [26] Robert D. Cowan and Donald C. Griffin, J. Opt. Soc. Am. **66**, 1010 (1976).
 [27] Robert D. Cowan, *The Theory of Atomic Structure and Spectra* (University of California Press, Berkeley, 1981).
 [28] I. P. Grant, J. Phys. B **7**, 1458 (1974).
 [29] E. R. Brown, S. L. Carter, and H. P. Kelly, Phys. Rev. A **21**, 1237 (1980).
 [30] H. P. Kelly, in *Computational Quantum Physics*, edited by A. S. Umar, V. E. Oberacker, M. R. Strayer, and C. Bottcher, AIP Conf. Proc. **260** (AIP, New York, 1992), pp. 131–141.
 [31] Charlotte E. Moore, in *Atomic Energy Levels as Derived From the Analyses of Optical Spectra*, Natl. Bur. Stand. Ref. Data Ser., Natl. Bur. Stand. (U.S) Circ. No. 35 (U.S. GPO, Washington, DC, 1971), Vol. III.
 [32] Leonard I. Schiff, *Quantum Mechanics*, 3rd ed. (McGraw-Hill, New York, 1968), p. 433.
 [33] K. N. Huang and A. F. Starace, Phys. Rev. A **19**, 2335 (1979).
 [34] Mitchel Weissbluth, *Atoms and Molecules*, Student ed. (Academic, New York, 1978).